Alexandria Engineering Journal 99 (2024) 137–167

Contents lists available at ScienceDirect

Alexandria Engineering Journal

journal homepage: www.elsevier.com/locate/aej

Review

Experimental investigation and finite element analysis of reinforced concrete beams strengthened by fibre reinforced polymer composite materials : A review

Solahuddin Bin Azuwa *, Fadzil Bin Mat Yahaya

Faculty of Civil Engineering Technology, Level 1, Chancellery Building, Universiti Malaysia Pahang Al-Sultan Abdullah, Lebuh Persiaran Tun Khalil Yaakob, 26300 Kuantan, Pahang Darul Makmur, Malaysia

ARTICLE INFO

Keywords:
Experimental
Finite element modelling
Fibre reinforced polymer
Composite material
Reinforcement
Reinforced concrete beams

ABSTRACT

As a composite material, fibre reinforced polymer (FRP) has many uses. Incorporating FRP composite material enhances the reinforced concrete beams' (RCB) performance, properties and behaviour as external reinforcement. A summary of how different FRP influences the RCB properties should be studied. This review paper discusses the use of FRP to reinforce RCB and briefly describes the topic. Previous experimental studies and finite element analysis (FEA) results showed that RCB constructed with FRP significantly improved the axial load, load-deflection, ultimate load, crack propagation, stress-strain distribution, and failure mode of RCB. Since this FRP composite material has superior strength, force, mounting and anchoring properties, it can be used as an alternate exterior reinforcement in RCB. The structural behaviour and performance of RCB can be enhanced by utilising FRP composite material in civil and structural engineering, especially in building construction projects.

1. Introduction

Commercialisation research has generally increased since 1980 [1]. Fibre reinforced polymer (FRP) composite material has been developed as internal and external reinforcements to reinforce pre-stress and non-prestress concrete structures in Europe regions such as the United Kingdom, United States, Canada and the like [2–4]. In 1990, Japan explored magnetic levitation to support reinforced concrete structures by bringing FRP reinforcement to the forefront of the country's scientific community. In 1996, Japan was the first Asian country to develop the FRP reinforced concrete design manual guidelines [5]. The number of construction projects employing FRP as structural reinforcement has increased considerably, and many worldwide institutions have also developed FRP design standards [1,6]. Reinforced concrete buildings that need to improve corrosion resistance or electromagnetic translucence employ FRP as external reinforcement support.

FRP can also be used as externally bonded reinforcement to reinforce steel, timber, masonry, and concrete [7]. Infrastructure ageing and the need to modify structures to satisfy the FRP design criteria have reached the maximum structural component rehabilitation and strengthening for decades. At the same time, seismic retrofitting has grown gradually, especially in areas prone to earthquakes. Exterior bonded FRP has been increasingly used in strengthening and retrofitting beams, slabs and columns due to its superior light weight, strength, chemical resistance, and ease to use. These FRP strengthening methods are in the highest demand since they can be rapidly implemented and need human resources to support these methods [1,8]. Most current usage of FRP can be found in civil engineering, specifically in the construction of buildings, bridges, maritime structures, and many more. This review study assesses the FRP's mechanical properties, including its compressive, shear, flexural, and tensile strengths, by reviewing its design, matrix composition, and material characteristics.

The flexural and shear responses of fibre reinforced polymer reinforced concrete beams (FRPRCB) beams have been the primary focus of most previous research. Research on the fibre impacts on FRP-strengthened beams is urgently needed in the context of retrofitting older structures. This review study analyses and discusses the usage of FRP composite material in reinforcing reinforced concrete beams (RCB). In order to fully appreciate the potential of fibre materials, this article also includes the strength improvement data for freshly constructed RCB reinforced with FRP composite material. This review article will also dig into the relevance of FRP composite material technology by discussing the experimental study and finite element modelling (FEM) of RCB strengthening by FRP composite material. NM is used to do the

* Corresponding author.
E-mail address: solahuddin.08@yahoo.com (S. Bin Azuwa).

https://doi.org/10.1016/j.aej.2024.05.017
Received 5 September 2023; Received in revised form 23 January 2024; Accepted 4 May 2024
Available online 11 May 2024

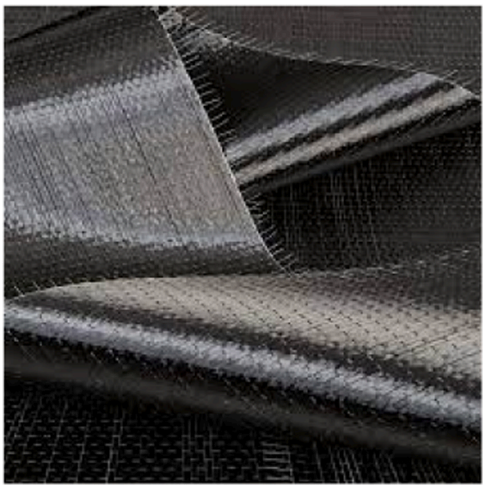

Fig. 1. Fibre reinforced polymer (FRP) composite material.

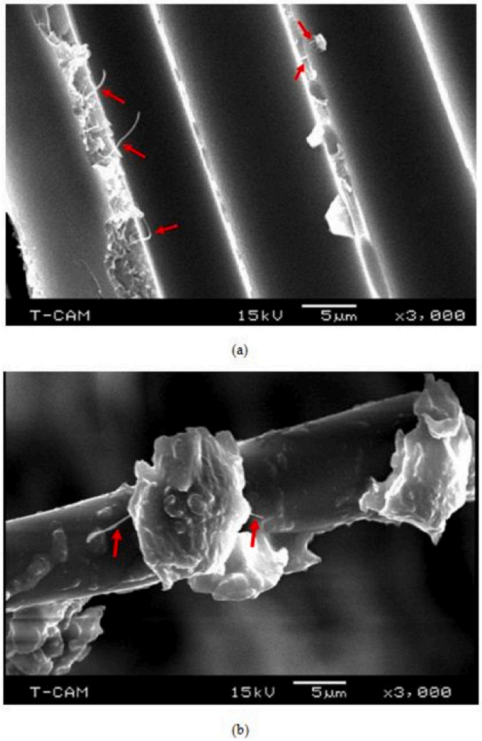

Fig. 2. SEM of FRP [10].

simulation and analyse the experimental results.

2. Fibre reinforced polymer composite materials

When combining two or more materials, the resulting composite material often has unidentical properties as the original components [9]. The features of FRP composite material are fibres, resins, interfaces, fillers, and additives. The mechanical qualities of FRP are enhanced by the fibres in the FRP matrix composition, which has high stress-strain and modulus of elasticity. Resins protect the fibres from mechanical and environmental degradation by transferring or distributing the stresses imposed on them. It is well known that the interface between the fibres and the matrix may safely affect the performance of FRP composite material. Fillers are added to concrete mix to increase cost-effectiveness and reduce shrinkage control. The fresh, physical and

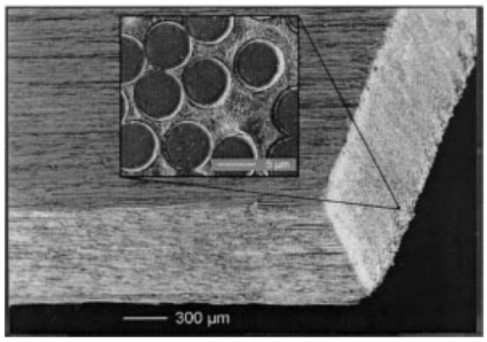

Fig. 3. 300 µm magnified FRP [11].

mechanical properties of composite structure are enhanced by FRP reinforcement [10]. FRP is extensively used in civil engineering and are typically made from one of four different materials: carbon, glass, aramid, or basalt [8,10–13]. The stress-strain for carbon, glass, aramid, and basalt FRP is different because they have different properties.

FRP bar is made by pultrusion process of impregnated thermoset resin fibres [11]. FRP is not influenced by chloride-induced solution since it is a naturally non-corrosive and non-metallic material. It also has the potential to improve the corrosion resistance of structures significantly. FRP is more durable, stronger, corrosion-resistant, and lightweight than regular steel. Nevertheless, its failure strain and elongation rate are low because of its linear elastic mechanical property without an obvious yielding stage. Also, except for some FRPs with high young modulus, their elastic modulus is often lower than typical reinforcing bar steel reinforcement. Reinforced concrete using FRP can be utilised in various forms like rod, tube, sheet, plate, roving, textile, and mesh fabric. Fig. 1 shows the FRP composite material.

3. Scanning electron microscope of fibre reinforced polymer composite materials

Fig. 2(a) is a high-magnification scanning electron microscope (SEM) micrograph revealing a remarkable bridging effect between long FRP fibres, carbon nanoflowers (CNF), and their matrices. Since CNF has a high aspect ratio, it is resistant to fracture and crack propagation, which boosts its efficiency. Fig. 2(b) shows that the resin is located on the top layer of FRP fibre, where the inclusion of CNF improves the adhesion bond. The interfacial adhesion strength is higher than the matrix strength in nanophase composite, which makes sense that the polyester can adhere to the FRP fibre surface. These images show that CNF has a strong resin and fibre anchor, which improves the interfacial bond between the fibres and their matrices. The strength of nanocomposite has increased due to better fibre-matrix interfacial bonds and the fracture development and propagation resistance provided by CNF [10]. However, the nanophase composite's modulus of elasticity is enhanced once CNF is mixed into the mix. This enhancement is because the matrix of these composites has become stiffer. The interfacial area between the resin matrix and CNF increases because of the CNF's high aspect ratio, enhancing the mechanical structural properties. In composite material systems, the nanoparticles also serve as reinforcing elements by carrying the load imposed. CNF and fibres are outperformed in terms of their matrix strength. When a load is imposed on a composite material, the matrix will crack earlier before CNF and FRP long fibres. This incident occurs because of the transferred stress from low modulus to high modulus of CNF and FRP long fibres via bridging effect [10].

FRP consists of a fibre phase that is dispersed within continuous matrix phases. High-stress areas can be reinforced to the fullest extent by bonding fibres in a certain position, direction, and volume in the polymer matrices. The FRP external reinforcement can potentially become a homogeneous member's minimal low-stress value. Furthermore, this FRP composite material has various advantages that make the building

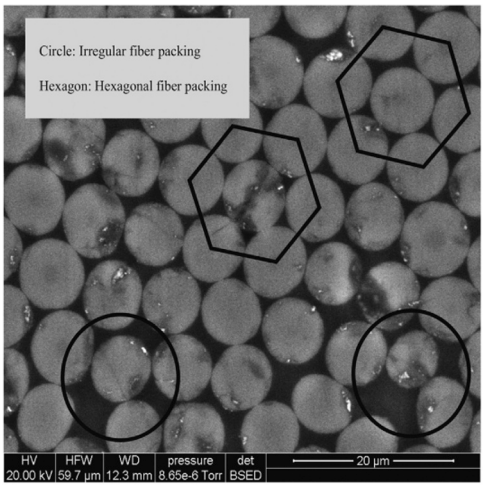

Fig. 4. SEM of FRP [12].

more efficient, such as decreased weight, carbon footprint, increased corrosion resistance, durability, and transparency. In Fig. 3, a magnified cross-section of FRP reveals the strip of FRP with a thickness of about 0.9 mm in one direction, situated at the strip's midpoint [11]. The fibres are approximately 6 mm in diameter and have a strip's longitudinal strength of 3400 MPa.

The fibre packings of FRP in Fig. 4 are taken by a scanning electron microscope (SEM). The dark backdrop indicates polymers, whereas the brilliant bright circles denote FRP with a diameter of around 9 mm [12]. The circles and hexagons depict the uneven and almost perfect fibre packings, respectively. This image is taken in a region rich in fibrous material to draw attention to the frequent occurrence of nearly perfect hexagonal packings [13]. Due to the observed variation in fibre packings and volume fractions within an area smaller than 110 microns, assuming perfect microstructures with an average fibre volume fraction as a starting point is a terrible assumption, even for wide averages. This divergence from the usual was also reported by numerous researchers [14–31]. FRP has been widely used because of its lightweight durability and versatility. The representative volume element (RVE) is used in most methods and techniques in predicting composite behaviour since it is similar to material microstructure. Typical RVE is based on idealised fibre packing layout variations such as square, hexagonal, or diagonal with 10% average fibre volume. Hexagonal and square fibre packings in their respective configurations are displayed in Fig. 5.

4. Experimental investigation of fibre reinforced polymer reinforced concrete beams

The results of the experimental study on the structural efficiency of fibre reinforced polymer reinforced concrete beams (FRPRCB) are reviewed in this section.

4.1. (Chin et al., 2011) [32]

The details of the beam specimens used in this study are listed in Table 1.

The beam strengths increased when using FRP in both round and square apertures. All the three tested beam experimental results are presented in Table 2. CB, C-cfrp-f, and S-cfrp-f had different maximum

Table 1
Beam details [32].

RCB	Type	FRP availability
CB	None	No
S-cfrp-f	Square	Yes
C-cfrp-f	Circle	Yes

Table 2
Experimental results [32].

RCB	Ultimate load (kN)	Failure type
CB	116.78	Flexural
S-cfrp-f	87.18	Shear
C-cfrp-f	175.51	Shear-flexural

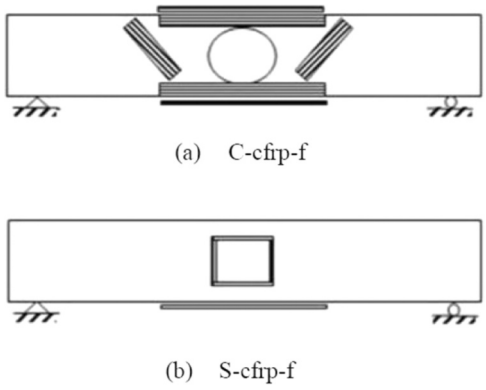

Fig. 6. Opening types (a) Circle (b) Square [32].

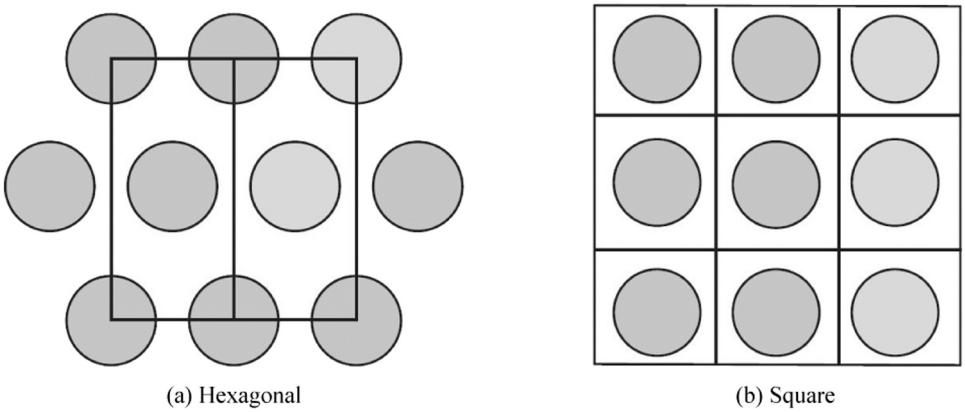

Fig. 5. Fibre shapes [13].

Fig. 7. Shear failure [32].

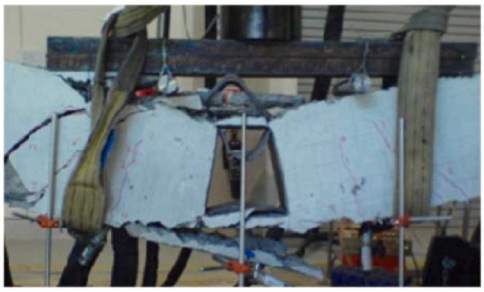

Fig. 8. Flexural failure [32].

loads (Pu) of 116 kN, 165 kN, and 87 kN, respectively. Compared to CB and S-cfrp-f, C-cfrp-f had the greatest Pu. The huge circular hole improved the flexural strength more than the massive square hole. This improvement was due to FRP fibre contents in the beam with a circular aperture. There was 43% improvement in strength compared to CB's ultimate load. As depicted in Fig. 9, C-cfrp-f and Scfrp-f's load-deflection behaviour followed the same pattern of stiffness as CB. In the post-yielding stage, C-cfrp-f delineated more ductility than S-cfrp-f. The beams were strengthened by FRP. When FRP was used as external reinforcement, fractures appeared in the flexural beams' tension zone beyond the prohibited region. Beam failure at midspan developed diagonal cracks as the fracture widths widened. Shear failure, as displayed in Fig. 7, occurred when the diagonal fractures developed, surrendered the bottom reinforcement, and rapidly crushed the concrete near the beam support. The beam cracks diagonally propagated around 16 mm in width. FRP was used to reinforce the square aperture in S-cfrp-f. During the beam test, flexural fractures appeared outside the FRP reinforcement area. As the number of cracks grew, some spread along the beam's neutral axis, while the remaining cracks developed on the diagonal close to the beam support. The diagonal fracture grew larger as it progressed towards the stress source until the beam failed in flexural, as observed in Fig. 8. The FRP started to crack near the beam support, and concrete crushing occurred. Moreover, fractures in the applied load region compromised the top chord of the aperture corner. As the main longitudinal bar yielded above the beam opening, it caused an abrupt concrete crushing. The FRP on the top and bottom of the aperture's inner surfaces was twisted and delaminated because of tension and compression stresses generated by the imposed load over the beam. Beams with circular openings were more robust than square openings. It was possible that the beam tension was first concentrated in one of the four corners of the large square opening. C-cfrp-f's ultimate capacity was increased due to the appearance of diagonal FRP next to the huge circular hole. The diagonal laminates prevented normal crack propagation from occurring. Thus, the cracks had to reroute through the unreinforced section without FRP, which required a great energy potential. The flexural fractures could locate the unreinforced area not under the FRP's control because of the square shape aperture in S-cfrp-f, causing the

Table 3
Sample details [33].

RCB	FRP availability	FRP attachment
1	Available	-
2	Non-available	Bottom
3	Non-available	Upper
4	Non-available	Support
5	Non-available	Point load

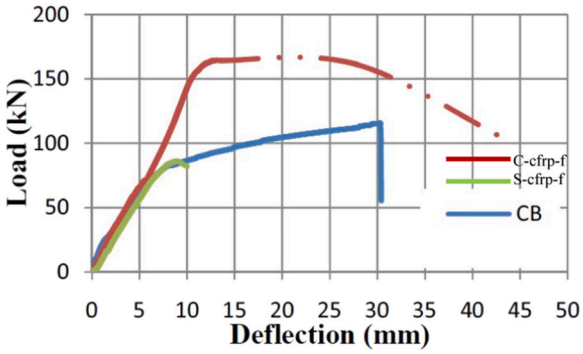

Fig. 9. Load-deflection [32].

beam performance to decline. An effective strengthening configuration might be produced by declining the extra strength given to C-cfrp-f and inclining the ultimate capacity imposed to S-cfrp-f.

4.2. Issa and AbouJouadeh (2014) [33]

The beam specifications details utilised in this research study are shown in Table 3. Fig. 10 shows the beam strengthening methods.

All five beam samples were presented. The enhanced load capacity of each beam type had been demonstrated. As seen in Table 4, the increased occurred in load capacity as the percentage was substantial. The stress levels of beams 2–5 were 34%, 71%, 70%, and 83% higher than the control beam. All beams were same under the same loads. Furthermore, the increase in the beam's rigidity stood out as one of the most distinctive features of each beam specimen. When comparing the fifth beam to the first beam under varying loads, the deflection data showed that the FRP-reinforced beam members were three times more than the original beam without FRP reinforcement. Each beam sample displayed pre-cracking, cracking, yielding and crushing stages. The fracture propagation severity was lessened as additional FRP laminate layers were utilised. Fig. 11 demonstrates that when extra FRP anchoring and wrapping were added, the beam specimens' shear bond, flexural strength, and duration for the reinforced strengthened component destruction inclined. The best and most applicable beam strengthening method used FRP as external support and reinforcement. Besides that, the stiffness and load-bearing capability of the beam were also improved when FRP was utilised as external main reinforcement. Using a lot of FRP laminates made the beam structural components stiffer and more resistant to being crushed or failing unexpectedly. The beam's performance and maintainability metrics increased as well as FRP anchoring was incorporated into the beam. These results showed that the strategic use of FRP laminates owing to anchoring, rigidity, and stiffness consideration improved the beam's strength, structural performance, and behaviour.

4.3. Abbood et al. (2021) [34]

Epoxy bonding with parallel fibres was practically possible in significant tensile stress that might be used to create shear reinforcement for RC structural components. Half or full wrapping of FRP depended on

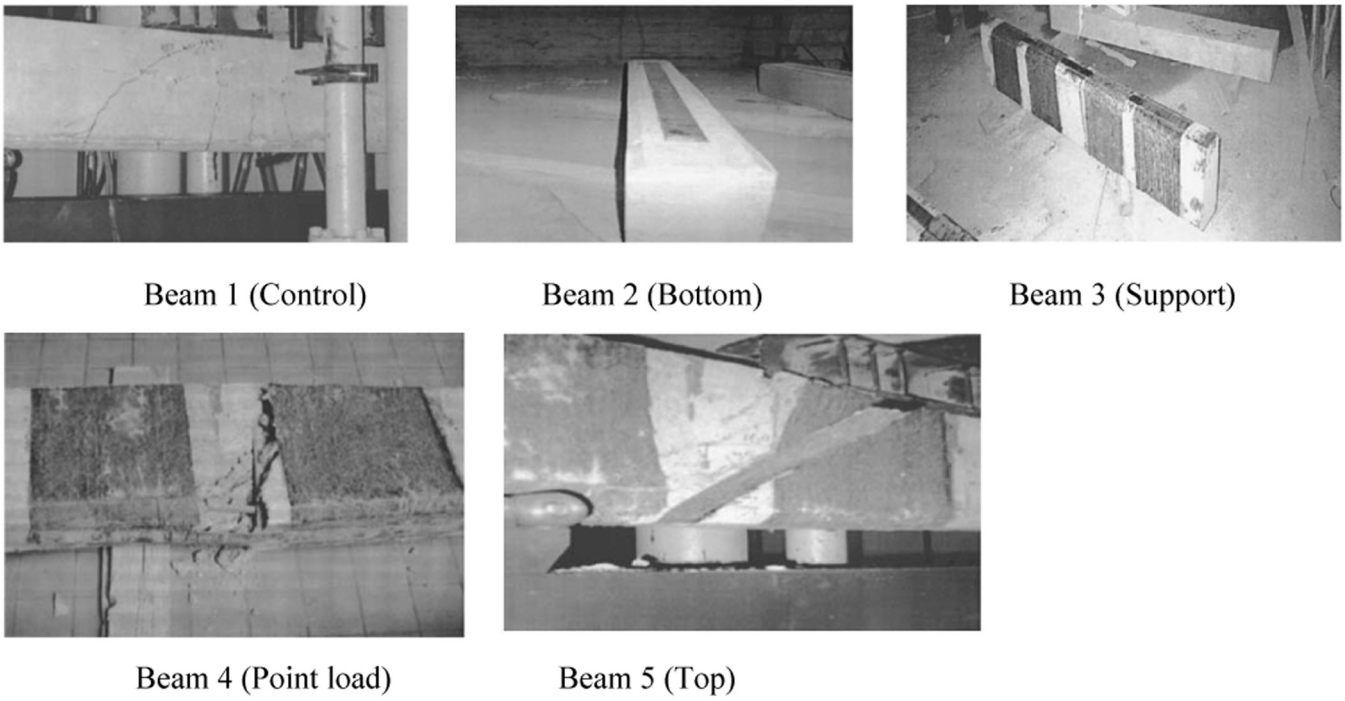

Fig. 10. Beam strengthening methods [33].

Table 4
RCB's load-deflection [33].

RCB	Load (kN)	Deflection (mm)
1	134	9.9
2	175	5.78
3	221	3.35
4	219	4.31
5	235	3.03

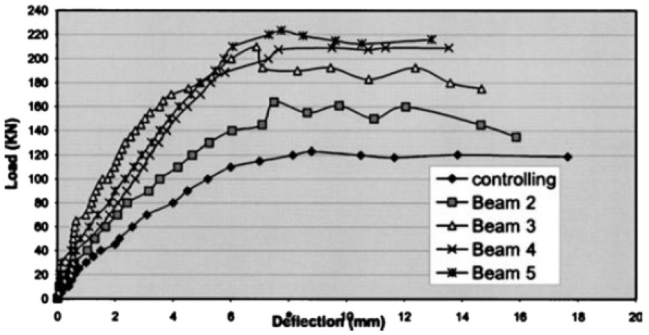

Fig. 11. Load-deflection [33].

the material accessibility to construct and strengthen the reinforcements. Epoxy's ability to soak up moisture reduced the shear strength in RC components. However, FRPRCB required stirrup spacing to sustain and retain shear loads or the concrete strength to shear loads must be relied on with the variable load imposed on the beam. Most FRP rebars' stiffness, stress, strain and elastic modulus were particularly low. The necessity for deep components or additional reinforcement to decrease fracture widths and alleviate long-term deflection occurred with low FRP stiffness characteristic. Three standard techniques were used: ACI 318, ACI 440, and ACI 318. All these three techniques were utilised for designing FRP shear strength, unallowed dowel movement action for FRP rebar to sustain shear force, and improved shear resistance for steel rebar. The FRP was designed to reveal the distinct load-strain contour at 45° orientation to increase the maximum efficiency of the beam shear strength. Moreover, the strain gauge reading depicted that the FRP sheet generated high shear strength with low shear fracture.

FRP-reinforced parts were typically over-reinforced, meaning a high proportion of FRP bars existed. Accordingly, the structural member failure was due to concrete crushing. FRP rupture failure mechanism occurred when the concrete reinforcement ratio was lower than the balanced ratio. Due to insufficient ductility in FRP failure patterns, the flexural strength decrease factor was between 0.6 and 0.7 based on reinforcing ratio. 0.55 was the strength drop factor for FRP rupture at failure point. There were two types of FRP reinforcing ratios: neutral and potential. The potential reinforcing ratio was 1.5 times higher than the neutral reinforcing ratio, causing the strength to increase to 0.66 when a destructive concrete failure occurred. The flexural strength of FRP-wrapped section was influenced by delamination factor. The higher the delamination factor, the lower the flexural strength. FRP bars did not have the same characteristics as steel rebars, producing different yield strengths. Moreover, it was expected that rupture strain for FRP composite material had capped flexural aptitude for reinforcing area. Flexural strengthening was accomplished by FRP reinforcing bonds with other materials like concrete, masonry, plate, and timber. Several studies had investigated various parameters and variables that affected the strength of FRP composite material, such as fibre length, binder bond factor, heat and cold treatments, and fibre pre-activation. The flexural members were strengthened to increase 50% load bearing capacity.

FRP, which was comprised of synthetic fibres in polymer matrices, created enormous tensile strength in a 90° perpendicular direction to fibres. It was used internally and externally to reinforce and strengthen RC structures. Straight, parallel, and continuous were the FRP fibre matrix types. However, fractures will occur and bonding between concrete and rebar will be severely compromised if the radial bursting stress exceeds the concrete element's tensile strength. The FRP's tensile strength specifications typically considered the fibre types, matrix orientation, and contact section. The strength increased with a certain fibre-to-weight ratio. Nevertheless, CFRP showed the lowest weight, tensile stress, and strength than other FRP composite materials.

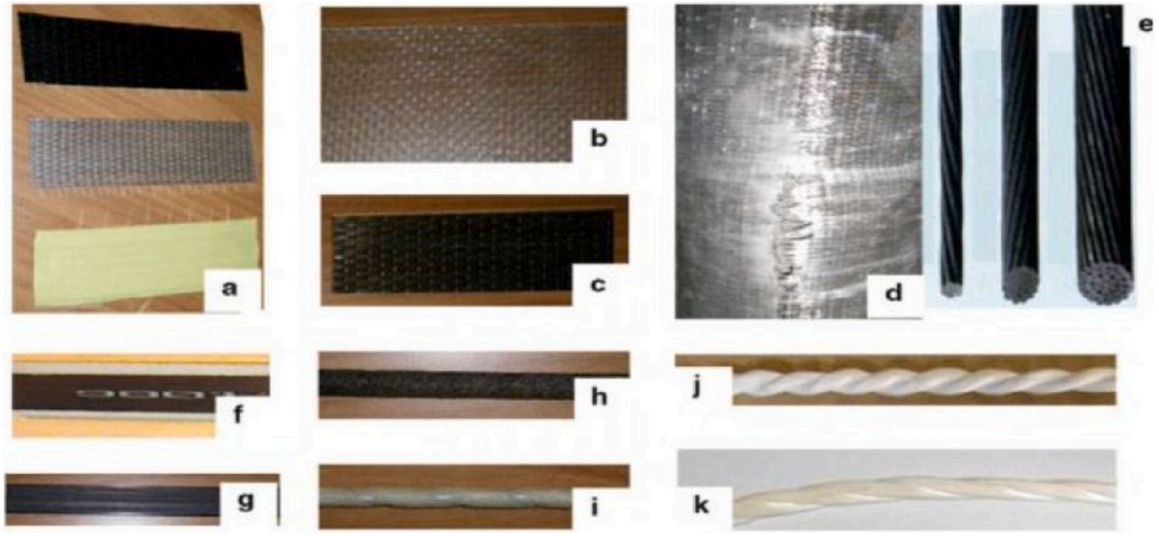

Fig. 12. FRP samples [35].

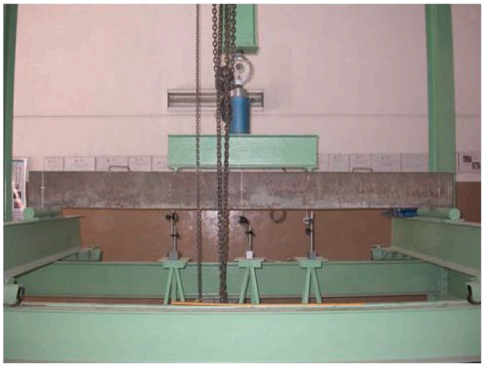

Fig. 13. Beam configuration system setup [35].

Considering that CFRP is an economically elastic-brittle composite material, this situation led to a notable decrease in weight and an increase in span for pre-stressed structural element. On the other hand, BFRP had excellent tensile strength and elongation at failure. The tensile strength of hybrid FRP inclined by 37%, which was bigger than the inclination shown when utilising PBO, which was just 3.7%. For GFRP made with vinyl ester, the tensile strength was shown to be only marginally affected by the investigation factors. Nevertheless, the tensile strength of GFRP made with polyester obviously declined by 90%. Rice and wheat husk were used as additive materials in CFRP and GFRP epoxy-based materials, reducing the strengths by approximately 23% and 20%. According to the results, hybrid GFRP had more diffuse tensile strength than CFRP and GFRP. In conclusion, GFRP was the best composite material than CFRP and GFRP. The experimental results for compressive, shear, flexural and tensile strengths of each beam sample type is summarised below.

Control RCB: 100, 110, 120, 130 MPa [34]
BFRPRCB: 200, 210, 220, 230 MPa [34]
AFRPRCB: 300, 310, 320, 330 MPa [34]
GFRPRCB: 400, 410, 420, 430 MPa [34]
CFRPRCB: 500, 510, 520, 530 MPa [34]

4.4. Siddika et al. (2019) [35]

Fig. 12 shows all FRP samples used in this study, while Fig. 13 delineates the beam configuration system setup. Two equal loads were applied to the beams, splitting the span into three similar lengths in order to test them under four point bending. Deflectometers were set up to measure the beam deflection. Two deflectometers with 200 mm spacing were attached to the beam's upper surface near the support to determine its curvature. The hydraulic jack was mounted on the spreader beam and used to measure the weight. A DEMEC gauge with four measuring pins spaced 300 mm measured the stresses at the beam's upper and lower surfaces. The deflection for each 3000 N load increment was measured in detail. Next, it applied the load monotonically. Other functions of the DEMEC gauge were to measure the rebar extension and the compression on the beam's upper surface. The readings of two dial gauges mounted on the beam's upper surface above the support were also recorded.

The near surface mounted (NSM) strengthening method could improve the beam's ductility and impart consistent flexural strength. Based on the results acquired, the flexural strengths of EB and NSM FRP-strengthened beams rose by 75% and 112%. Besides that, the composite strength was also improved by 67%. Several factors, including fibre choices, FRP insertion place, and concrete cover strength, determined the success probability of NSM strengthening method. This research also showed that 21% beam's ultimate moment capacity was increased by affixing the FRP-reinforced strips mechanically. The beams' flexural capacity was also involved in this research. Beams with CFRP and GFRP wrapping with three different concrete covers (30, 40, and 50 mm) were tested. The observed to expected bond strength ratio ranged from 97% to 135% for all possible permutations of concrete cover and wrapping conditions. The concrete cover thickness impacted the FRP wrapping strength. As three types of concrete cover thicknesses were used (30, 40, and 50 mm), 30 mm had the highest impact on the FRP wrapping strength, while 50 mm had the lowest impact on the FRP wrapping strength. The retrofitted beams' total strength was significantly increased after being strengthened with FRP. Replacing corroded steel reinforcement with BFRP strips raised the flexural strength, deflection bearing amount, ductility, and stress capacity by 15%, 16%, 17% and 18%, respectively. Furthermore, substituting deteriorated steel reinforcement with BFRP strips also increased the beam's load capacity by 36%. Thus, FRP composite material was the best and most brilliant choice for flexural strengthening, rehabilitation, and repairing RC beams. It all depended on the condition of the damaged beams and the material quality used to reinforce, rehabilitate or repair the RC beams.

Flexural failure is the most typical failure in RC beams. Most RC beams need to be reinforced to make them more durable and increase their service life. Reinforcement or retrofitting using EB and NSM FRP procedures could increase the flexural capacity of RC beam. Factors such

Table 5
Specimen details [36].

Sample	Composite	Ribbed type	Reinforcement ratio		Ultimate load (kN)	
			Longitudinal	Transverse	Predicted	Actual
S-1	C	Yes	2.24	1.68/1.2	10.6	10
S-2	ECC	Yes	2.24	1.68/1.2	15.3	13.6
S-3	ECC	Yes	2.24	-	15.3	15.4
S-4	ECC	Yes	2.24	-	15.3	14

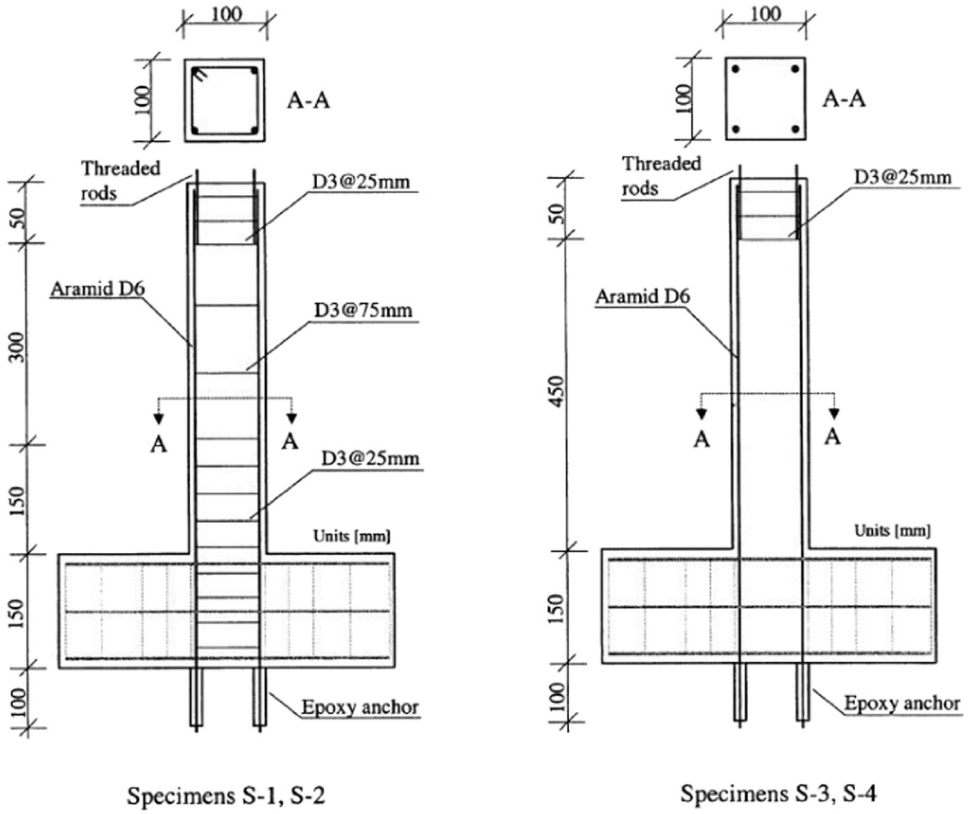

Fig. 14. Specimen configuration [36].

as material quality, strengthening method and applied load affected the RC beams' function. FRP laminates could be applied along the beams' tension face, influencing the beams' strength. U-wrapped and completely wrapped FRP beams showed impressive performance, although the latter was more difficult to implement. The flexural strength, stiffness, and load-deflection resistance of RC beams might all be improved by wrapping them with FRP in a U shape. FRP thickness affected the strength-to-weight ratio. Two layers of FRP sheets by the U-wrapped method influenced the beam deflection by reducing it to 40%. Beam weakening might occur if an excessive flexural reinforcement ratio is utilised. According to this study, u-wrapped hybrid composite beams comprising CFRP and GFRP layers could increase the beams' ultimate load strength performance by 104%. The FRP sheet and concrete were bonded with each other. It was crucial to the overall performance of the beam's structure. There were also premature bond failures that occurred in the RC beam. These premature bond failures, which were critical and brittle failures, could be lessened and even avoided by utilising intermediate anchoring, mechanical fastening, and NSM FRP strip strengthening.

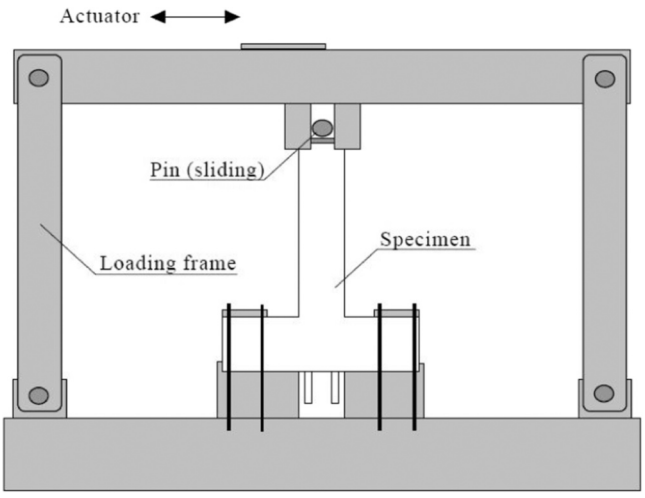

Fig. 15. Loading system [36].

4.5. Fischer (2020) [36]

Table 5 shows the summary of the specimen details utilised in this

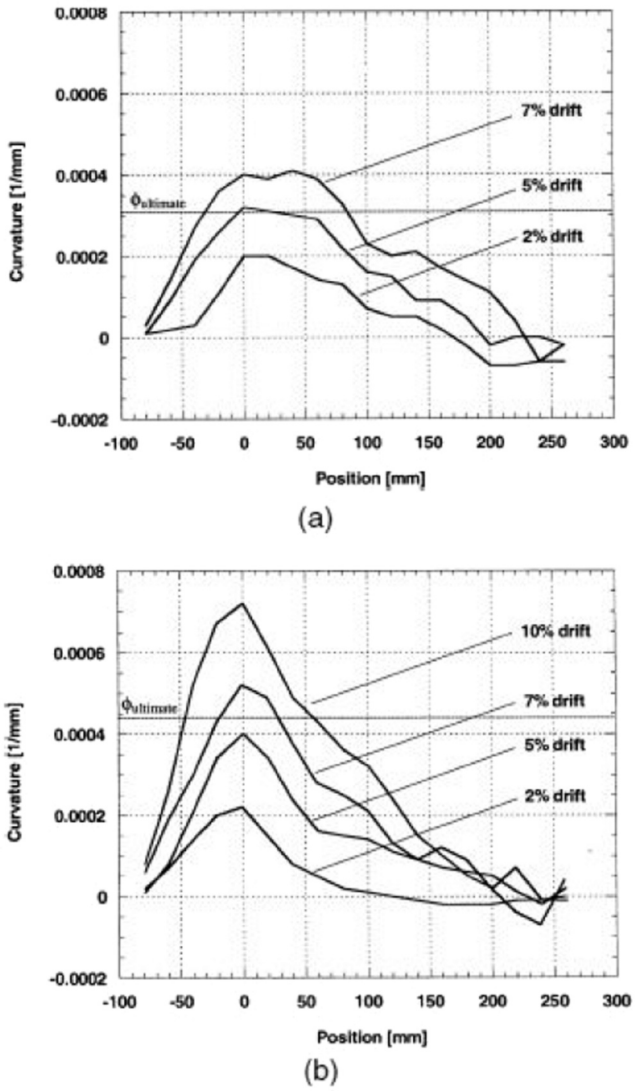

Fig. 16. (a) S-1 (b) S-2 [36].

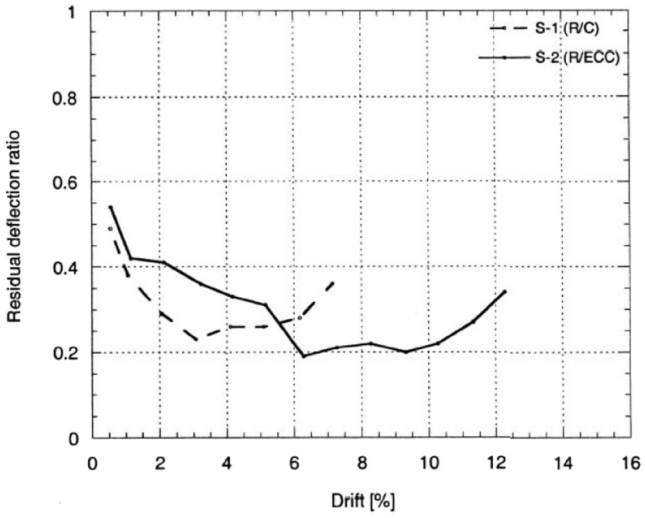

Fig. 17. Residual deflection-drift [36].

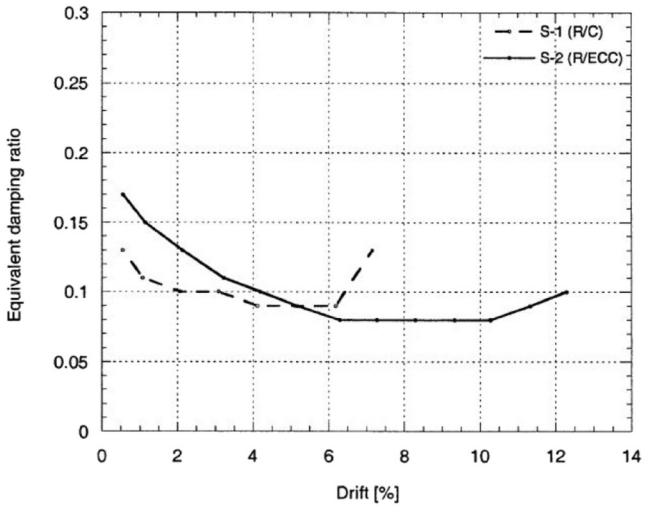

Fig. 18. Damping ratio-drift [36].

study. C stands for cementitious, while ECC stands for engineered cementitious composite. Figs. 14 and 15 show the specimen configuration and loading system. The experimental investigation and comparison of the structural behaviour of FRP-reinforced ECC flexural members with FRPRCB was carried out using small-scale cantilever beams with dimensions 500 mm tall and 100 mm^2 cross-sectional area (Fig. 4). A stiff transverse beam was cast integrally with the cantilever beam base to provide a similar loading condition. The outside anchoring of longitudinal FRP reinforcement used epoxy to produce strong sticking and bond. Fig. 6 delineates that the transverse beam was tightened to the loading frame base and a steel pin was placed on the upper surface in order to support lateral force. There was a lack of vertical restraint for the loading pin. A displacement transducer was installed on the cantilever upper end to ease recording the entire displacement. Black-coloured lines were spray-painted on the beam surface to make the deflected form of the beam easily measured by using the image processing method.

Between the joint area and the 260 mm sample height, the curvature distributions of S-1 (Fig. 16(a)) and S-2 (Fig. 16(b)) are shown at increasing drift levels. The slight curvature at these portions and the low resolution of the digital figures greatly impacted the accuracy of data acquired at points above 260 mm. The massive curvatures at the cantilever base were identical for both samples when the drift was set to 3%. The curvature dropped more gradually in S-1 as it moved upwards along the cantilever, whereas it lowered faster in S-2 as it moved downwards. The difference was more noticeable at 6 and 8% drifts when the FRP-reinforced concrete composite curvature was practically constant at 70 mm cantilever base height. At 7% drift, the predicted theoretical and observed peak ultimate moment-curvature relationships for S-1 were 0.00042/mm and 0.00050/mm before failure. S-2 measured peak curvature more prominent than the expected value, same as S-1. S-1 and S-2 were compared across a range of drift velocities regarding their residual deflection (Fig. 17) and energy dissipation (Fig. 18). The higher the drift level, the lower the ratio. S-1 and S-2 produced 0.2 ratio values. At 4% drift, flexural fracture saturation was detected in S-1, while in S-2, the minimum residual deflection was recorded at 7% drift. After this stage, the deflection in S-1 increased rapidly due to inelastic deformation process. The residual deflection ratio in S-2 was maintained at a constant 0.2 ratio beyond the drift level at which the flexural fracture saturation was achieved, considering a stable and continuous flexural deformation process to occur. Above 10% drift, the deformation process significantly shifted from compression to bond breaking, considerably increasing the residual deflection ratio. The patterns outlined could be seen in the energy dissipation characteristics for both S-1 and S-2 samples. Besides that, S-2 exhibited larger residual deflection prior to flexural crack saturation because of the greater number of

Table 6
11 specimens [37].

Beam	Number of samples	Dimension (mm)	Exposure duration	Test type	Test standard	Loading type	Loading rate (mm/min)
Control	7	252 ×26×4	-	Uniaxial tensile	ASTM D4140	Displacement control	3
Exposed	6	253 ×26×44	5 months	Uniaxial tensile	ASTM D4140	Displacement control	3

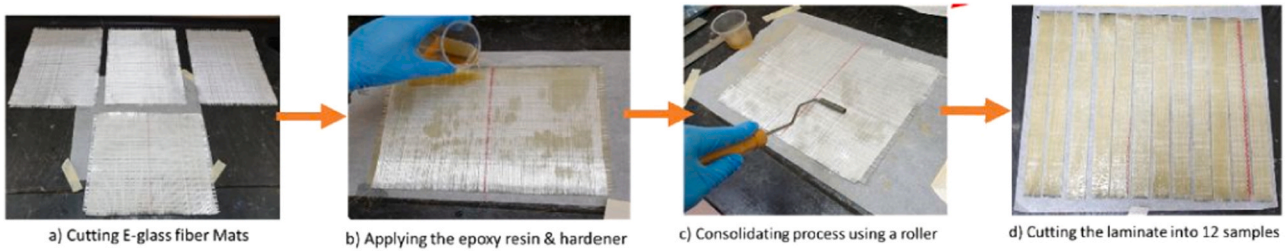

Fig. 19. GFRP sample preparation steps [37].

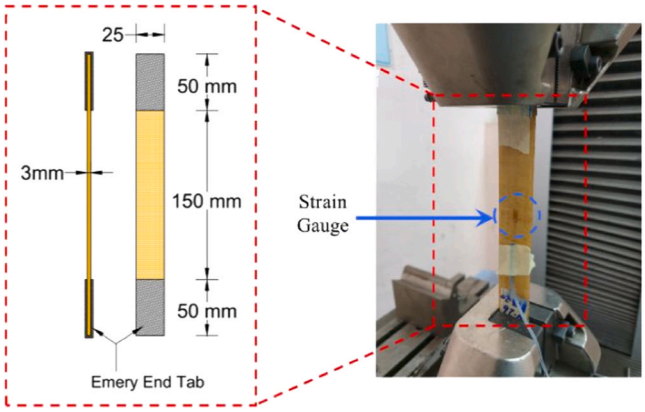

Fig. 20. Tensile test setup [37].

flexural cracks than S-1.

In contrast to the curvature concentration at the base properties of steel-reinforced components in inelastic deformation regime, the curvature distribution in both samples suggested that the elastic behaviour gradually declined along the beams' cantilever. The sample's moment distribution and sectional flexural stiffness strength influenced the sample's curvature variation throughout its peak. As a result, the S-1's consistent curvature indicated that the debonding and detachment of the concrete around the reinforcement led to a constant stress variation distribution at the FRP external reinforcement. In contrast, the S-2's curvature distribution kept its downward slope at all drift levels, especially at the beam's lower base. This downward slope was retained because FRP maintained its integrity and the mechanical bond between elastic FRP reinforcement and ECC matrix. This disparity might be attributed to confinement effects of transverse reinforcement, which inclined the strain capacity of cementitious matrix beyond the values anticipated in moment-curvature equation.

This study defined residual deflection as the difference between the highest deflection acquired at a specific drift level and the constant deflection after unloading. Identical damping ratio measured energy dissipation by dividing the total energy lost by the total elastic energy stored in the beam's span at a specific drift level. The flexural fracture development predominantly affected the specimen behaviour at low drift levels for deflection and energy. There is an unusual residual deflection ratio at 1% drift, primarily due to the fracture closure being unfinished after unloading at a low drift level. The corresponding damping properties and residual deflections were minimised when the flexural cracks were saturated for a particular time. Internal friction

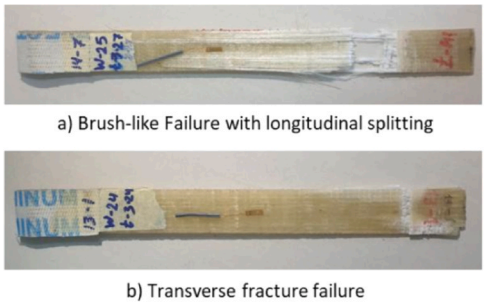

Fig. 21. Control specimens [37].

maintained the deflection and the damping ratio from changing when the deflection increased over the saturating level. A slight rose in deflection and damping was the final damage outcome caused by fibre crushing and rotational sliding. Based on the findings, it seemed that the results of FRP-strengthened components were significantly impacted by shear and flexural crack developments as well as the damage generated by tension-compression failure. However, it could maintain its flexural deformation mode beyond saturation with slight deflection until an overwhelming drift level.

4.6. Mousay et al. (2021) [37]

Table 6 shows all 11 specimens used in this study, while Figs. 19 and 20 show the GFRP sample preparation steps and tensile test setup. A universal testing machine (UTM) capable of withstanding a direct tension load was used to test eleven GFRPRCB samples. Five GFRPRCB specimens were exposed to tropical air conditions, while the remaining six control specimens were not exposed to tropical air condition. A displacement control method was used to conduct the direct tension test at a 2 mm/min rate following ASTM D3039 standards [23]. Each

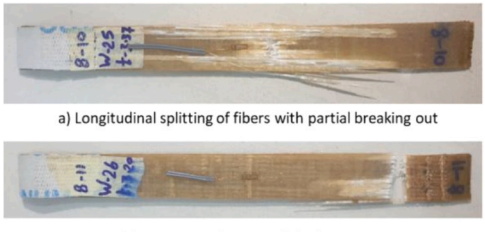

Fig. 22. 4 months exposed specimens [37].

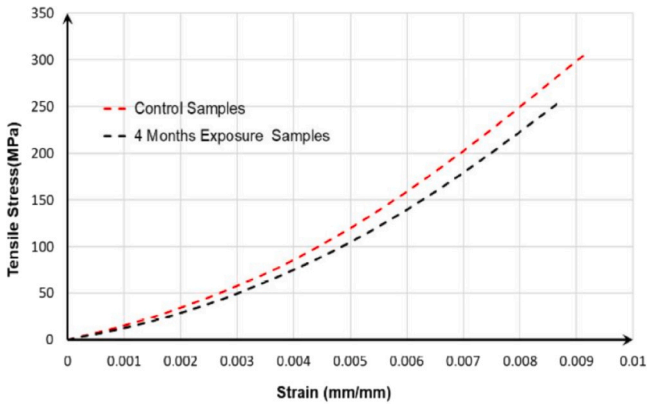

Fig. 23. Tensile stress-strain [37].

Table 7
Tensile strength and young modulus [37].

RCB	FRP type	Environment type	Tensile strength (%)	Young modulus (%)
A	E-poxy	Tropical	16	5
B	Isophthalic	Seasonal	19	6
C	E-glass	Urban	15	44
D	Vinylester	Scorching hot	4	35

GFRPRCB had a strain gauge attached to its centre location to measure the strain values. The applied displacement, load response, and strain response data were recorded throughout the test.

Brush failure, characterised by lengthy fibre splitting, was a prevalent failure mode for the control sample, as shown in Fig. 21(a). This type of failure was uncommon in old or damaged substances. Two samples showed transverse failure with a clean cut in the matrix and the woven glass fibre mat (Fig. 21(b)). Tensile failure for four air exposure samples occurred within the gauge length, as shown in Fig. 22(a), due to several interlaminar cracks in the same direction of the longitudinal fibres, resulting in splitting tensile failure without total fracture. However, one sample in Fig. 15(b) exhibited a transverse failure mode characterised by a fibre clean cut. Fig. 23 displays the stress-strain relationship for the untreated control sample and the sample exposed to the air atmosphere for four months. The ultimate tensile strength of GFRP was 318 MPa and reduced to 273 MPa after exposure to tropical conditions for several months at room temperature (28 °C). 22 GPa with 5% increase were recorded for the modulus of elasticity of GFRP samples. The strain modulus increased, but the strain failure decreased due to specimen swelling under air exposure. Additionally, the samples subjected to standard atmospheric conditions had 0.0091 strain failure, 15% lower than the sample value evaluated under control conditions. Table 7 compares the results of the present and previous studies that have been concluded in the literature review based on FRP types, in-situ environment, highest exposure period, declination in tensile strength, and modulus of elasticity. Under the influence of winter seasonal conditions in Switzerland, the tensile strength of GFRP decreased by as much as 19% after 8.5 years of exposure. Subsequently, for Portugal and Malaysia, the GFRP lost their tensile strengths at 15% (3.5 years) and 16% (4 months) after being exposed to the urban environment. Nevertheless, GFRP exposed to the natural ageing urban environment in Portugal delineated a significant loss of modulus of elasticity, with 34% and 25% reductions in Young Modulus for E-glass/polyester and E-glass/vinyl ester. In contrast, two other countries, Switzerland and Saudi Arabia, showed no appreciable loss in modulus of elasticity. No noticeable loss in modulus of elasticity occurred in Switzerland and Saudi Arabia because Switzerland was a cold country with below −5 °C temperature. At the same time, Saudi Arabia was a scorching hot country with over 30 °C temperature. Overall, the comparisons showed that the site conditions in various worldwide regions could generate varied deterioration of the FRP tensile characteristic.

Table 8
Beam samples [38].

RCB	Dimension (mm)	Predicted failure
B4	64 ×35×21	Shear
B5	64 ×35×21	Tensile
B6	66 ×35×24	Tensile
B7	66 ×34×22	Tensile
B8	64 ×35×21	Tensile
B9	64 ×35×22	Compression

Inadequate integral load transfer capability might occur if water penetrated the fibre material during exposure, causing the fibre matrix interface bond to degrade and declining the transverse fibre resistance. The variation in the data around the mean of all samples was represented by standard deviation, which followed a plus-minus sign. The ultimate tensile strengths used as controls and those exposed to the air were average calculated to get their tensile strengths. Moreover, Young's modulus was considered the gradual slope of the stress-strain curve. Both stress-strain curves were almost linear until the failure point, suggesting that GFRP was fragile. Furthermore, the GFRP stress-strain curve clearly showed how air exposure affected the tensile strength performance over five months, with the GFRP samples displaying low tensile stress up to failure. Synergistic damage from moisture penetration and temperature variations were likely to be blamed for this weakening since they altered the fibre matrix connection.

4.7. Springolo, (2015) [38]

Table 8 depicts the beam samples used in this study. Figs. 24 and 25 show the beam cross-section and FRP wrapping strengthening system. Structural Concrete laboratory was used to test the beam samples using loading frames. The objective was to measure stresses on concrete surface in shear zone along X-Y-Z axis, as seen in Fig. 4. The surface strains were measured using a hydraulic gauge with a minimum value of 1/100 strain units. Unfortunately, the flat surface of the wrapped beams made it impossible to identify the demec points. Also, any scratching of the beam surface would damage the FRP wrapped. Thus, as illustrated in Fig. 5, an electrical resistance gauge with a 40 mm gauge length was applied to the wrapped beams' surface to measure the surface strains on two surfaces. The two surfaces were shear span, which ran in fibre direction and constant bending moment region, which ran perpendicular to fibre.

The analysis method correctly anticipated that the beam bulks would fail due to the bottom laminate's tensile rupture. In Fig. 26, the strain behaviour of all beams was very identical. The behaviour remained linear and elastic until the initial tensile failure of the core material occurred. Moreover, the tensile strains behaved non-linearly when the load rose, but the compressive strains were relatively invariant because of varying tensile moduli in the core material. It was clear that the ultimate tensile strain corresponded to a tensile strain of around 0.7%. Fig. 27 displays the average moment-curvature graphs, which reveal the reason for the reduction in beam stiffness. During the experimental test, the audible indicators of cracking occurred until the material failed. L/30 was the average ratio equivalent to 20 mm deflection. Beam B7 used in this experiment had a symmetric shape. 5 of 10 tested beams were installed with strain gauges. The analytical technique overestimated the average failure moment by 11% with 2.411E6 N.mm value acquired. The analytically tensile strain predicted agreed with the actual values (S1-S5) shown in Fig. 28. Fig. 29 delineates the average failure moment of 2.436 E6 N.mm. All strains predicted by the analysis were in the range within 5% of the measurements (Fig. 30). As seen in Fig. 22, the faster the load applied to the beam, the quicker the changing of the

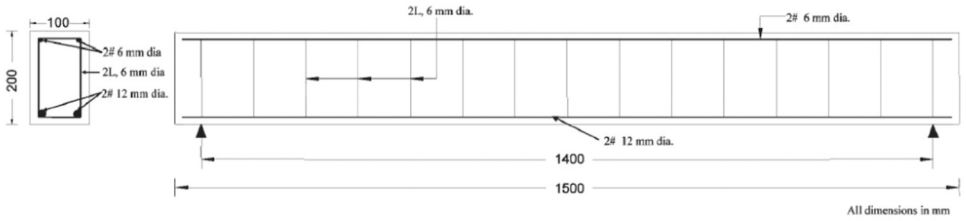

Fig. 24. Beam cross-section [38].

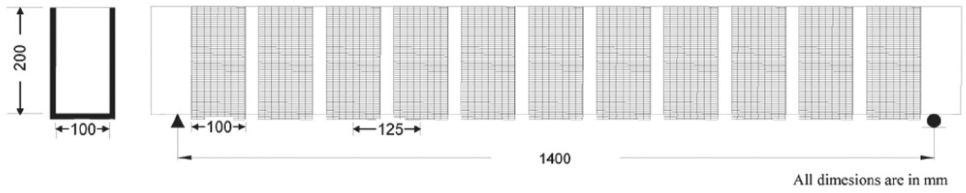

Fig. 25. FRP wrapping scheme [38].

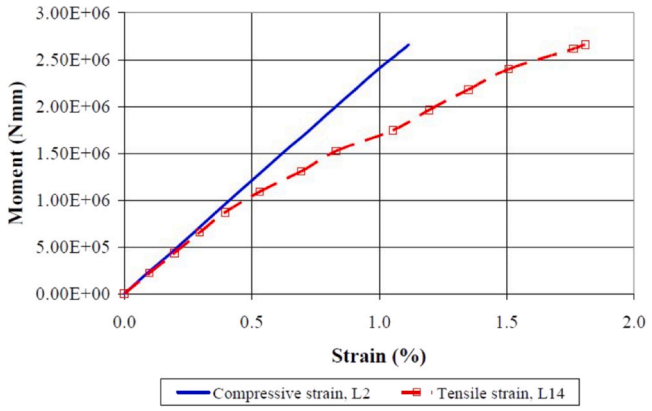

Fig. 26. Moment-strain [38].

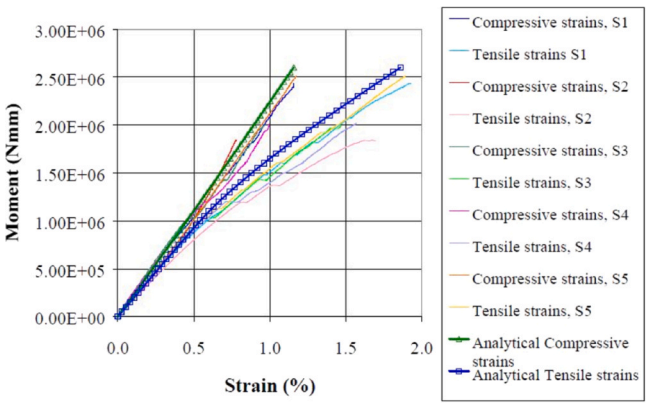

Fig. 28. Moment-strain (B7) [38].

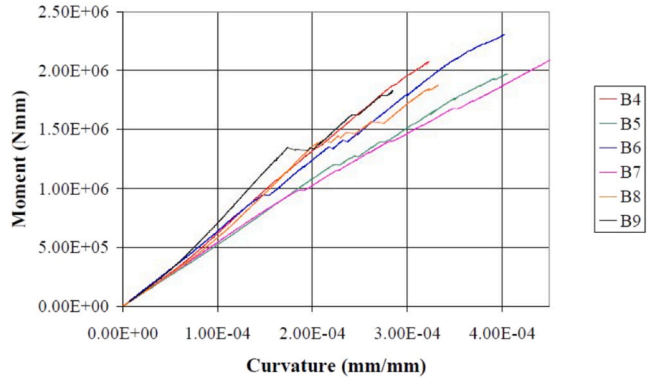

Fig. 27. Moment-curvature [38].

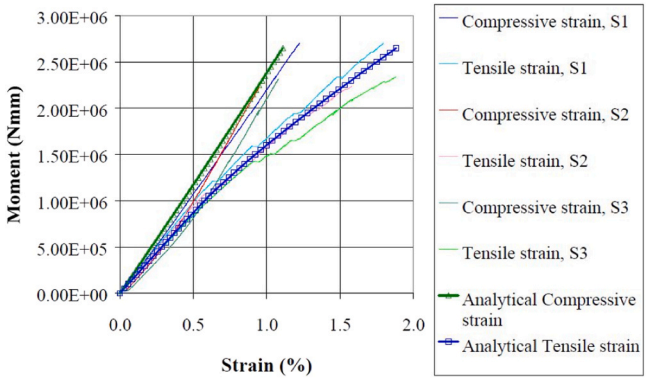

Fig. 29. Moment-strain (B5) [38].

compressive stress. This compressive stress change was because of beam buckling. Fig. 31 shows a difference in tensile strain that occurred when the core material in the tensile flange reached its strain value limitation.

The B5 in second series core material in the bottom flange was intentionally decreased during production. The beam failure occurred due to unidirectional laminate rupture because the tiny quantity was enough to withstand the second order of shear punching in bottom laminates. Despite the analytical method's apparent simplicity, it accurately forecasted a failure moment of 10% higher. Also, all findings from the strain models were within 10% of the experimental values. The tests conducted in B8 had the least core material in top flange, revealing that the reduced amount of core material was enough to resist bearing stress and provided appropriate compressive reinforced constraint. All beams broke at stress areas. The strain gauge recorded 2.22 Nm standard failure moment. The actual average maximum failure moment was 80% more than the analytically predicted. Upon closer inspection, the beams were discovered to have crimson stains within the unidirectional FRP laminates. The fresh batch of unidirectional FRP laminates used for the

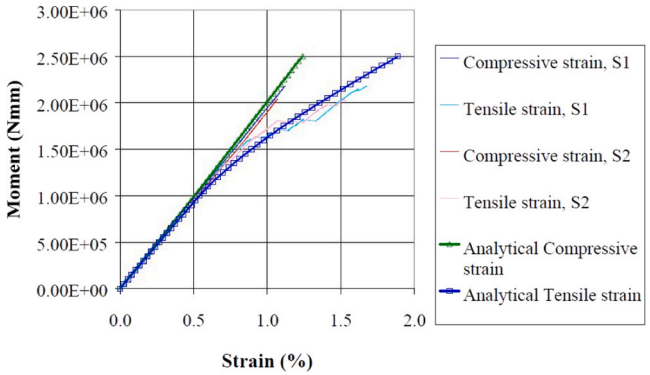

Fig. 30. Moment-strain (B8) [38].

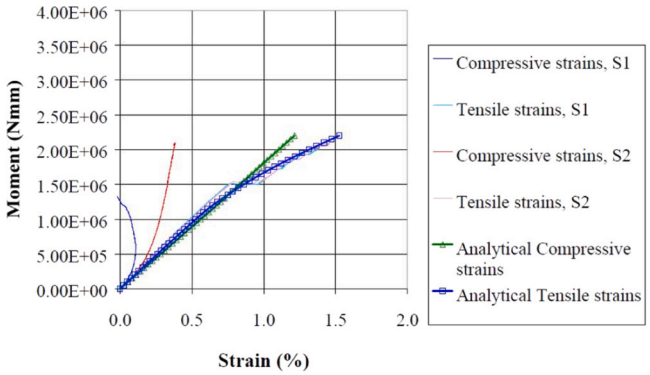

Fig. 31. Moment-strain (B9) [38].

Table 9
Specimen test details [39].

Group	Specimen	Shape	FRP ply (Inside)	FRP ply (outside)	Total FRP ply
A	1	Circular	0	0	0
	2	Circular	3	4	7
	3	Circular	5	7	12
	4	Circular	7	10	17
B	1	Square	0	0	0
	2	Square	3	4	7
	3	Square	5	7	12
	4	Square	7	10	17

beams had a crimson thread that caused discolouration. After further testing, it was determined that this batch of unidirectional FRP laminates had a failure capacity reduction of 13%. Incorporating FRP laminate caused the failure strain to incline 6% more than the typical beam without FRP laminate.

Compared to tensile equivalents, the compressive stresses at failure were consistently lower throughout all experiments. The FRP laminates had a greater modulus in compression and the flange incorporated a core material. Thus, the FRP beams produced were immune to primary compression failure of unidirectional laminate. The beams in B9 series prematurely collapsed due to lack of compressive restraint because there was no core material in the top flange. The first buckling in the laminate occurred under a constant loading point, suggesting that the bearing pressures were also involved. 2.05E6 N.mm was the average failure moment recorded. These failure breakdowns showed how vulnerable the top flange to load configuration. This caused a rapid transfer of loads along the unidirectional reinforcement path. However, the beam absorbed the released energy due to ample unidirectional reinforcement. The average bearing failure rate anticipated by the analytical

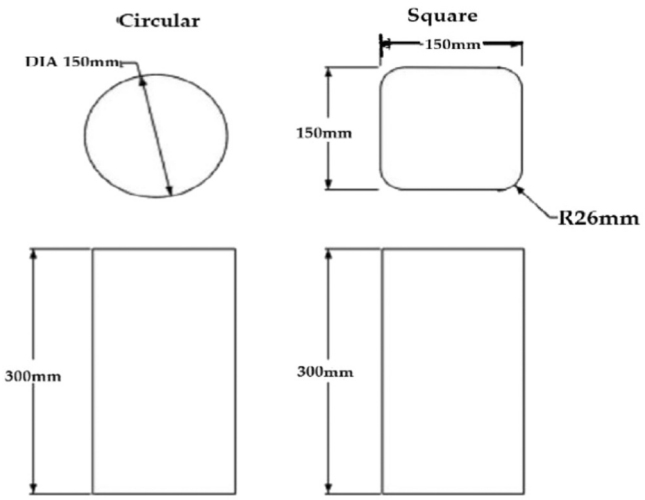

Fig. 32. Dimensions [39].

Fig. 33. Loading system [39].

model was 9% bigger than the value acquired in the experiment. 5% was the tensile strain analytical prediction within the actual value.

4.8. Polymer et al. (2019) [39]

Table 9 depicts the specimen test details utilised in this research study. Fig. 32 delineates the circular and square specimen dimensions, while Fig. 33 illustrates the loading system utilised in this research study. The concentric axial compression loads were monotonically increased on all square and round concrete columns until they failed using UTM, having 3000 kN load capacity. Two 10 mm high-strength steel plates matched the square and circular cross-sectional shapes at the end of the concrete columns. Both shapes had a 26 mm radius measurement. This step ensured that the load applied would only affect the concrete core. 0.3 mm/min permanent displacement rate was used to test the unconfined samples. In contrast, 2 mm/min loading rate was maintained for the confined specimens due to high predicted axial displacement. The constrained concrete reaction was unaffected by any variations available in this loading rate. The data logger TBK-640 was linked to a computer, recording the test data from LVDT and load cell.

The lateral distortion of concrete core under decisive axial compressive stress action failed because JPFRP confined circular

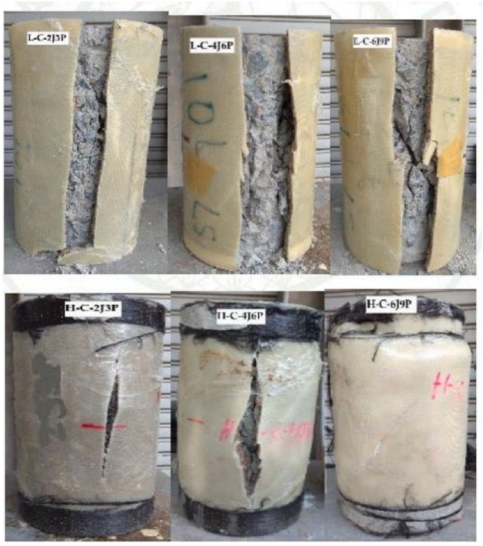

Fig. 34. Circular columns [39].

Fig. 35. Square columns [39].

concrete specimens' low strength due to JPFRP laminate cracks. When the JPFRP laminate cracked, it caused the concrete columns to break suddenly and become brittle with an explosive noise. The cracking sound was intermittently heard prior to the breakdown, indicating the linear breaking of the inner FRP sheets. As delineated in Fig. 34, the JPFRP shell fractured along the sample surface with a long crack propagated vertically from top to bottom. The crack that emerged was parallel to axial compressive stress and perpendicular to the orientation of JPFRP confining layers. Previous studies also reported a similar failure pattern. The failure mechanisms of declined and inclined strength for square specimens are illustrated in Fig. 35. The 15 layers H-S-6J9P showed no cracking signs. Massive rupture strain of FRP polyester fibre restricted the corners' sharp movement. H-S-6J9P demonstrated lateral bulging and predominance of great strain capacity of FRP polyester fibre in hybrid confinement. The final axial deformability of concrete rose, as well as the increase of FRP layers utilised. 15-layer FRP specimens were so soft and flexible in one way, parallel and perpendicular directions.

When the concrete core fractured, the JPFRP laminate containment was triggered, stopping the lateral expansion from becoming wider. However, transverse strain in the JPFRP shell was caused by lateral growth in circular columns. The FRP shell ruptured and finally failed when it reached its final state. High-strength concrete column delineated a significant failure compared to other specimens. No audible crack or minor vertical fracture spread as the concrete was reinforced with

Table 10
Specimen details [40].

RCB	Dimension (mm)	Compression steel	Tension steel	Stirrup spacing	RCB scheme
A	160 ×260	5H35	5H35	180	Simply supported
B	160 ×260	5H35	5H35	210	Continuous
C	160 ×260	5H35	5H35	180	Simply supported
D	160 ×260	5H35	5H35	210	Continuous

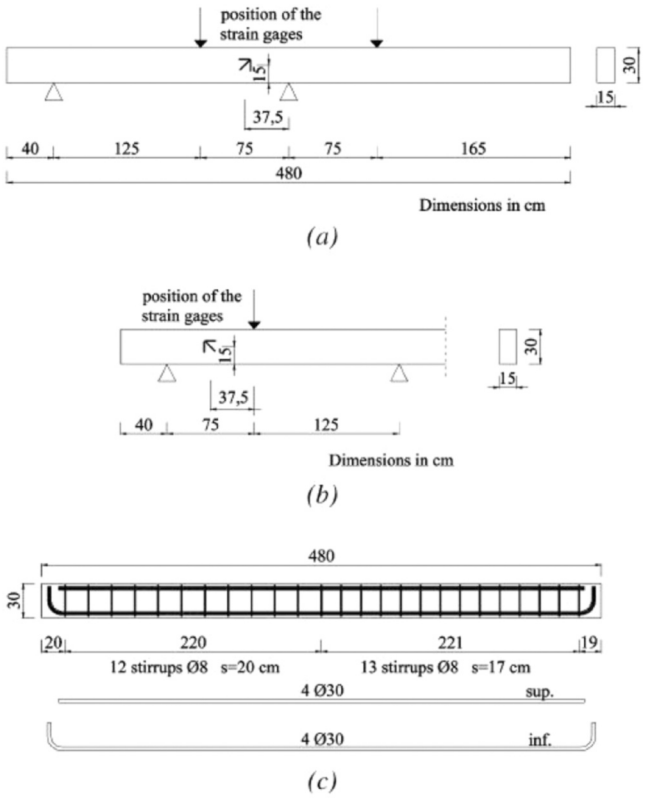

Fig. 36. Specimen and loading system [40].

JPFRP-confined low-strength columns. 20 mm of FRP had been wrapped around the specimen surface. The FRP was wrapped in high-strength circular specimens after seeing that they experienced less load drop than low-strength circular columns. Load drop still happened when peak strength was reached, but the failure mechanism of the specimens was shifted. H-C-6J9P laterally bulged without visible vision. Furthermore, there was a shift in the cracking pattern of high-strength specimens. Failure modes also occurred in circular samples. Based on the technique used, there was no debonding between jute and polyester layers, demonstrating a strong connection between fibres in FRP. A solid and durable interfacial connection was also acquired between the hybrid JPFRP shell and the concrete column surfaces. The failure pattern of hybrid JPFRP-confined concrete was rare and unique, unlike a concrete specimen wrapped in regular FRP composites like aramid, carbon, basalt, glass, and the like. FRP laminate also contained synthetic fibres, which caused the concrete to fail in various types, shapes, and sizes. Similarly, the square hybrid JPFRP confined concrete specimens also failed due to shell cracking. The FRP laminate ruptured vertically, from the middle surface to both ends. There was a sporadic snapping sound just before the FRP sheet broke, followed by a loud cracking sound. Ductile failures occurred in high-strength square samples, producing low collapse noise sound. Stress concentration affected the JPFRP square specimens by creating concrete failure around the specimen surfaces.

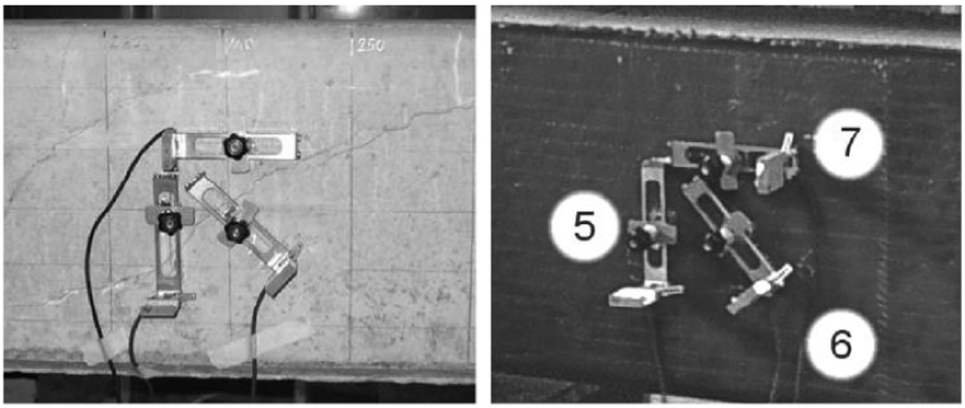

Fig. 37. Test setup [40].

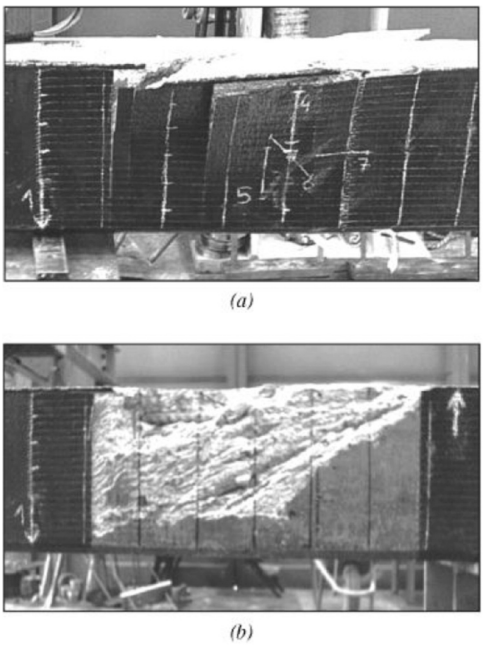

Fig. 38. (a) Strengthened beam (b) After FRP was removed [40].

Crushing and concrete disturbance caused by FRP crack were detected along the freed section of the specimen. Other research studies also had the same findings for the failure modes of JPFRP-confined concrete.

4.9. Pellegrino and Modena (2016) [40]

Table 10 explains the specimen details used in this study. Fig. 36 illustrates the specimen and loading system used. Three and four-point flexural tests were performed. A hydraulic jack capable of supporting 600 kN load was used, which was operated manually. The signals from the instruments were recorded using an automated data acquisition system. LVDT instrument was used to evaluate vertical displacements under applied loads. Moreover, additional LVDTs were placed over the beam supports to assess potential displacements. FRP stresses were additionally recorded in four distinct directions on the beams' vertical surface in order to estimate shear deformations in the crack zone. Fig. 37 demonstrates the apparatus used to measure deformations in control and shear-reinforced beams. Fig. 37(b) displays that the strain gauges were horizontally placed, 45^0 in longitudinal axis, and vertically oriented with numbers 5, 6, and 7.

Shear-reinforced FRP beams were now included in the model scope.

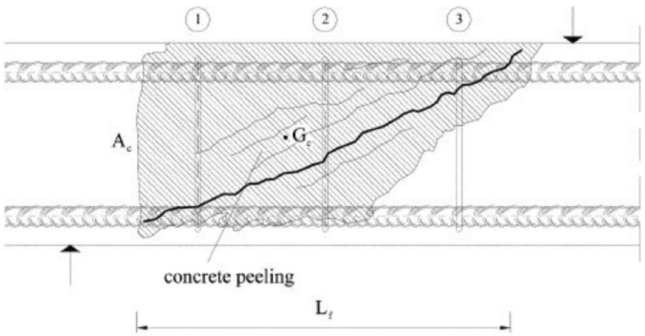

Fig. 39. Strengthened beam configuration [40].

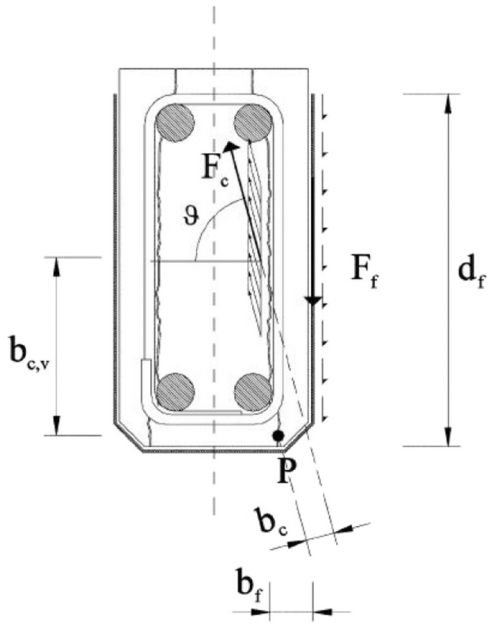

Fig. 40. Force action [40].

The hypothesis concluded that the rupture of the beam included the concrete cover separation along a vertical plane that had been postulated on the basis of experimental failure modes for all specimens (Fig. 38). The fracture of FRP was prevalent when a full wrapping strengthening strategy was typically used for U and V-jacketed beams. Internal deformations had been assumed to be similar to the corresponding observed deformation in exterior fibre, assuming there was no

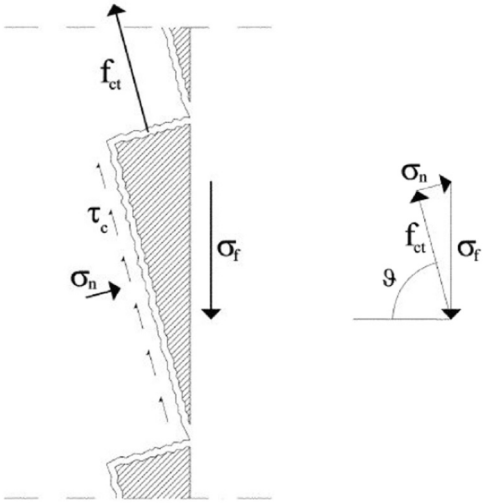

Fig. 41. Concrete geometry [40].

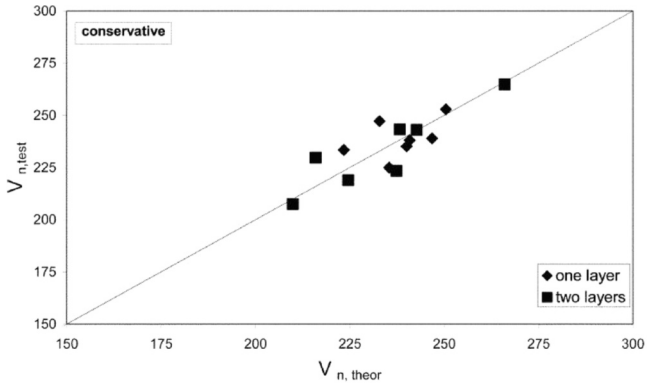

Fig. 42. Shear strength (experiment-theory) [40].

Table 11
Experimental results [40].

RCB	Vn_1 (kN)	Vf_1 (kN)	Vn_2 (kN)	Vf_2 (kN)
A	239	53	64	58
B	244	58	86	94
C	226	56	64	58
D	230	61	86	94

slippage between the substrate and FRP. The experimental parameters for determining the FRP shear force comprised the FRP active length, as referred to in Fig. 39. Lf and Ac were the symbols for peeled concrete between longitudinal FRP bars. An idealised representation of the forces acting on the lateral beam concrete cover related to friction action and tensile strength of RC is presented in Fig. 40. The fibre developed horizontal and vertical forces along its matrices. Fig. 41 depicts a simplified geometric illustration of peeling contact between the concrete core and shell. The angle defined the standard contact roughness as delineated. Fig. 42 compares the predicted shear strength generated from the current model to nominal experimental measurement. The results of further empirical examination for the comparable beams were also considered. The current model yield values were in close agreement with the experimental data. The shear-deformation diagram and the cracking pattern at failure overlaid on the stirrup arrangement were available for all beams. The model could be further endorsed using other experimental data. The difference in shear failure loads (Table 11) could be explained by different cracking patterns of simply supported beam

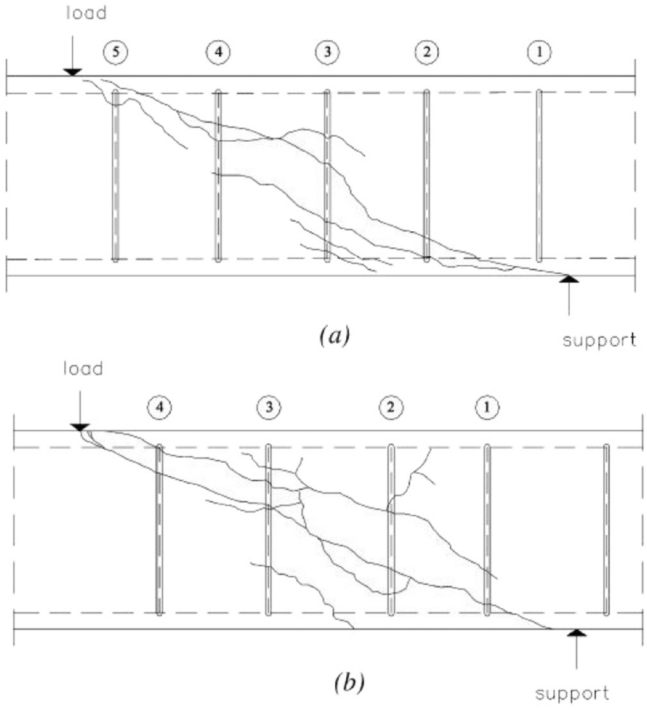

Fig. 43. Beam cracking patterns (a) Continuous (b) Simply supported [40].

compared to continuous beam, as seen in Fig. 43(a) and (b).

The analytical recommendation was typically unconservative, as seen in Table 11 and was consistently lower than the experimental values of FRP shear strength and contribution, including the data values produced from the current model. Eurocode and British standards assumed a 45-degree inclined diagonal fracture. This assumed 45-degree value caused the steel shear contribution to be always more than the value computed with conventional technique. Since the experimental nominal shear capacity could not be adequately approximated using Eurocode and British standards, the nominal shear resistance was calculated as a total of various contributions, which seemed well matched. On the other hand, the shear strength contributions were always partially and separately treated, even though they interacted significantly and benefited the FRP reinforcement strength. The beam deformation with one FRP layer was higher than the beam deformation with two FRP layers despite the beams having the same stirrup spacing. Besides that, reducing stirrup spacing but maintaining the same layer of FRP sheet affected the beam stress by declining its value. This might increase the credence of the theory that increasing FRP content might reduce the deformation in steel stirrup and steel shear connection bond. Steel web reinforcement and stirrup spacing were related to FRP deformation and shear strength. High steel web reinforcement with low beam stirrup spacing produced less FRP deformation and shear strength. This would explain why beams reinforced with two layers of FRP were more efficient than those beams reinforced with a single layer of FRP. According to another recent research, the shear gained by the FRP was a plateau at specific shear rigidity. The same stirrups spacing involved various partially and fully contributing stirrups intersected with the critical crack. The two static system resistances were gained due to FRP distinction, reducing the cracking patterns propagation. The presence of FRP as exterior reinforcement affected the beam's behaviour, such as cracking pattern, stress-strain distribution, nominal shear capacity, and failure mode. The change in cracking patterns was most likely due to the decrease in steel percentage for strengthened beam specimens and the apparent small resistance gained due to FRP shear strength for simply supported beam specimens. Less concern was taken for continuous beam samples.

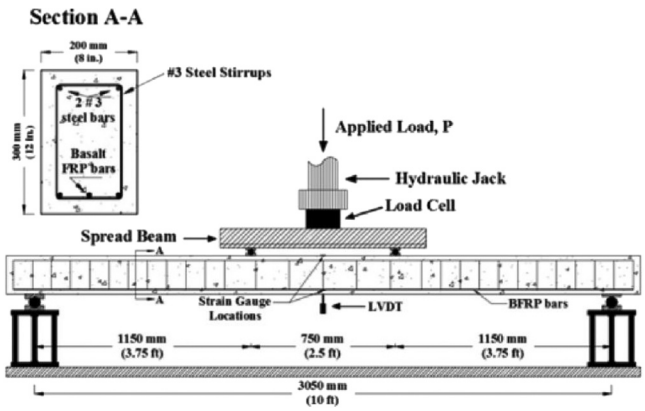

Fig. 44. Instrumentation setup [41].

4.10. Ovitigala et al. (2016) [41]

Fig. 44 illustrates the instrumentation setup. The beam test's load rate was ideally 7–10 kN per minute. A hydraulic jack under the beam's mid-span was used to produce the load, which was then transferred to a broad flange. The applied load was measured using a load cell attached to the hydraulic jack. In order to quantify the concrete strain, the strain gauges were attached to the concrete compression surface at the beam's mid-span. Furthermore, the strain gauges were installed under every FRPRCB's mid-span. LVDT measured and recorded the beam's mid-span deflections. The data from LVDT was collected using a 40-channel data logger device.

The concrete in each middle of eight BFRPRCB was crushed, as predicted in Fig. 45. Each one broke similarly when the concrete on the compression face was crushed. Fig. 46 shows the various breaking patterns seen in eight RCB and displays that the beam with a larger reinforcement ratio had fewer cracks and shallower fracture depths in constant moment area but had a deeper crushed section in compression zone at failure point. As shown in Fig. 47(b), the moment-deflection curve fluctuated after the cracks were formed, indicating the formation of additional cracks and the unchecked growth of the initial crack until the deflection reached a value of L/180. Fig. 47(a) illustrates that the beams exhibited less variation after breaking than the L-beams. In the post-cracking area, the moment-deflection behaviour of 3–13 M and 2–16 M fluctuated up to a deflection limit of L/360, while for 3–16 M, the moment-deflection behaviour varied before the deflection reached L/600 deflection limit. The post-cracking zone of M-beams was consistently elastic and stiff throughout the experimental investigation. The fracture propagation zones for 2–25 H and 3–25 H beams were smoothly transitioned. Due to massive reinforcement ratios, the moment-deflection curve slope was reduced without any variation symptoms when both beams fractured until they failed, as Fig. 47(b) delineated. Both 2–25 H and 3–25 H beams' moment capacities at L/180 deflection were 3–4 times greater than 3–10 L beam. More than half of the maximum deflection recorded in 3–10 L was eliminated due to FRP debonding and concrete crushing.

An inconsistency between experimental and theoretical cracking moments is demonstrated. This inconsistency was more significant for the former than the latter. The beam developed further flexural fractures along its length in permanent moment area when the initial cracking stress exceeded the expected value. As the load increased, the cracks propagation developed in shear area while the flexural cracks spread towards the beam top surface. Outside of the steady moment

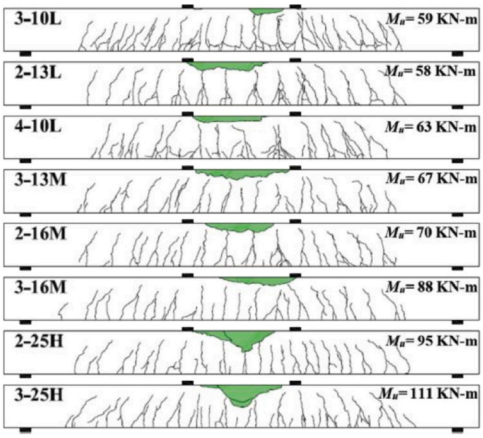

Fig. 46. Crack patterns [41].

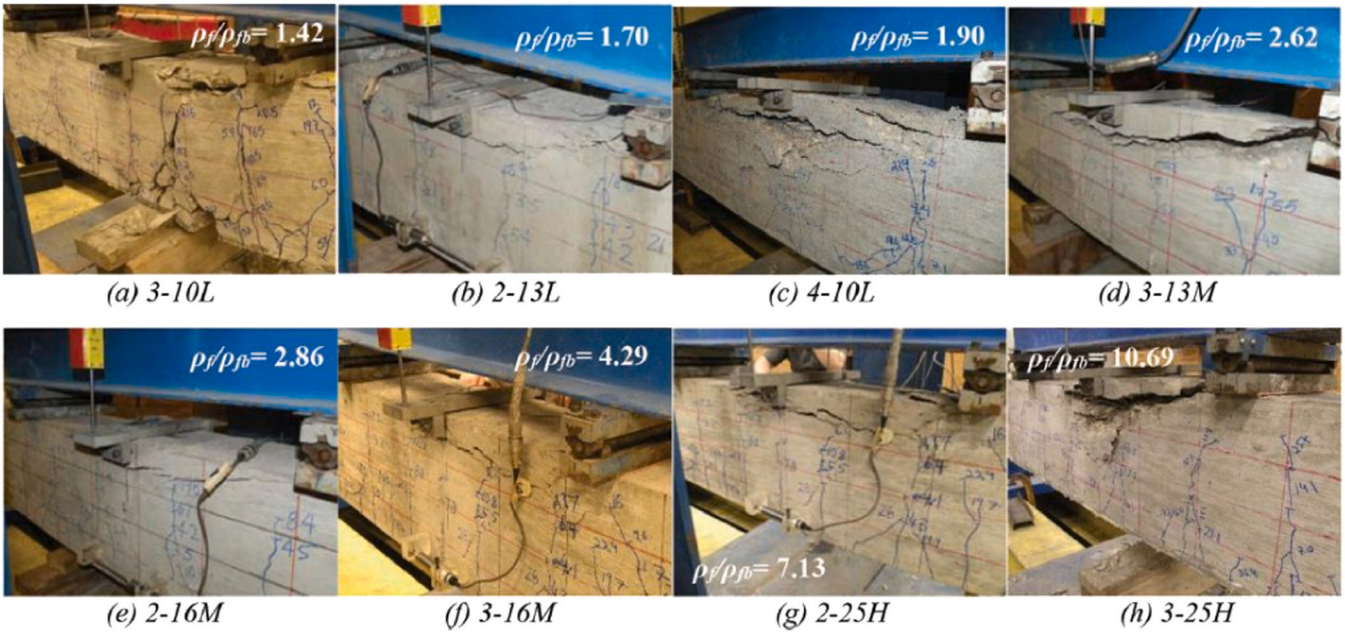

Fig. 45. Failure modes [41].

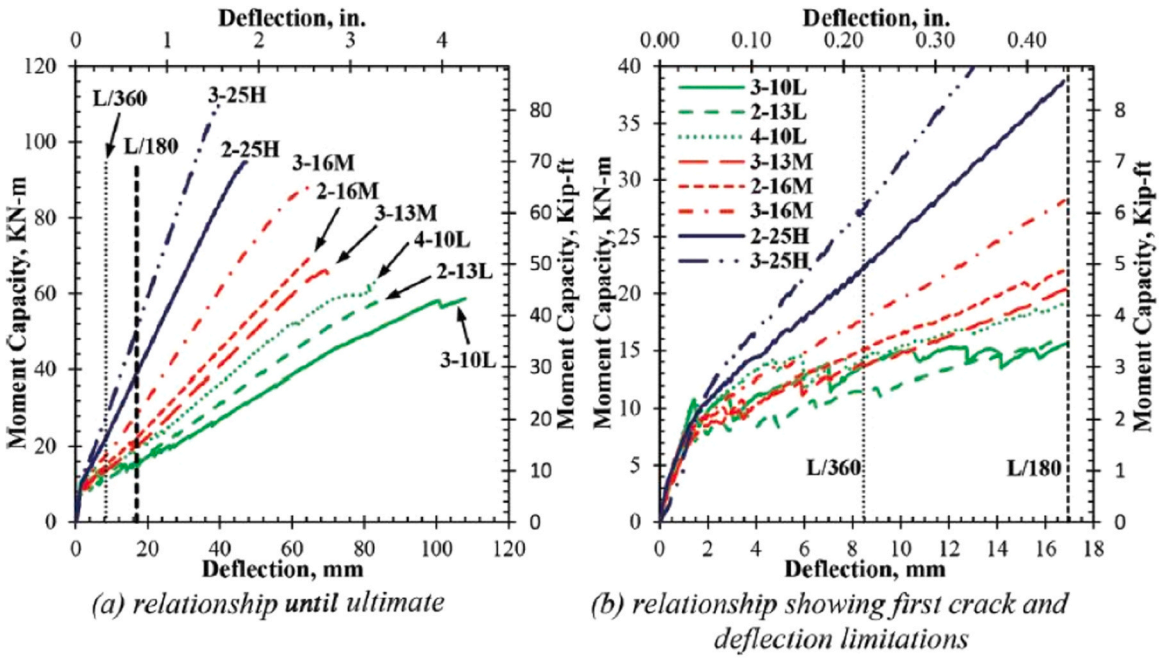

Fig. 47. Moment-deflection [41].

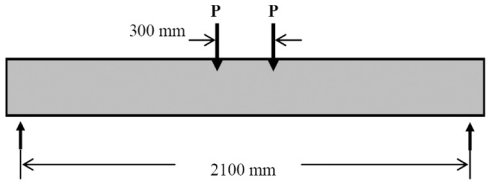

Fig. 48. Beam test setup schematic drawing [42].

development zone, the fractures were slanted. The beam bored the weight until the flexural capacity reached its maximum value. The concrete in constant moment area, including compression zone, was fractured at this point. Since the strain in the FRP bars did not approach the ultimate rupture strain, most of the deflection was recovered when the beams were unloaded after failure. This failure pattern was regular for FRPRCB, which had succumbed to concrete crushing. In addition, the beams retained a small degree of permanent deflection due to concrete crushing and bonding slippage between the FRP bars and concrete connection. This deflection inclination occurred in post-cracking region. The beams were evaluated in a load control setting, which caused these various variations. The beams also considered service loads in their design specifications. From the results acquired, L/180 deflection was the least conservative deflection limit compared to other deflection values. After passing this deflection threshold, the L-beams became more rigid, with moment deflection retained constant and straight. The moment-deflection curve was continuously monitored in L-beams until the maximum moment remained close to the tiny downward shift until the beams failed due to concrete crushing at the beam's upper surface.

4.11. Gudonis et al. (2014) [42]

Each beam was made in a controlled normal environment under 28 ^{0}C room temperature and was cast using plywood moulds. An electrical strain gauge was glued on the tensile reinforcement centre to quantify the tensile strain during load imposed. All beams were simply supported with an effective span of 2000 mm and tested at 28 days under a four-point flexural test. The beam centre was subjected to two-point loads with 300 mm spacing. Fig. 48 demonstrates the beam test setup schematic drawing. The beam parameters investigated were load-deflection, steel and concrete deformations, yield loads, crack patterns, failure modes and shear performance.

However, many research studies concluded that a shear-strengthening system made of FRP for RC beam reinforcement was successfully implemented. The FRP-reinforced beam's load capacity rose by 33%. Furthermore, the failure mode shifted from shear tension failure to shear compression failure and the deformability was 115% greater than the unreinforced beam without FRP. The pre-stress force from FRP reinforcement repaired the failure beam and increased the beam's load-bearing capability by 55–60%. Beams with inadequate shear reinforcement or fractured concrete would have a reduced shear capacity and need strengthening.

In recent years, EB FRP systems have been widely employed for shear strengthening of RC beams. Shear FRP web reinforcements could be applied to beams in various orientations and bonding methods, including horizontal, vertical, inclined, side-bonded, anchored, and U-wrapped. The shear strength of RC beams might be improved using EB FRP strengthening approach, which depends on the FRP reinforcement orientation types. The FRP layer, internal steel reinforcement types, concrete grade, and tensile steel strength had a role in the efficacy of shear strengthening employing EB FRP method. The approximation of EB FRP design for shear strengthening system was conservative because EB FRP could not be considered as internal stirrup reinforcement. Subsequently, the FRP yielding during concrete expansion fractures meant that the full internal stirrup strength could not be used to determine the load strength capacity. CFRP is a type of FRP. CFRP was utilised in an RC beam after high shear and flexural strengths were imposed on the RC beam surface until failure occurred. An external pre-stress force and a single U-wrapped CFRP layer sheet were used to seal the shear fractures in the failure beam. The pre-stress force was released right after the epoxy injection. Epoxy injection repaired the shear fractures before EB FRP sheet wrapping, which could significantly boost the final load capacity of the rehabilitated beams. The strengthening efficiency could be improved by using an average shear span-to-depth ratio, closed FRP spacing, and disregarding transverse load reinforcement. Hybrid FRP beam system performed better than conventional FRP beam system.

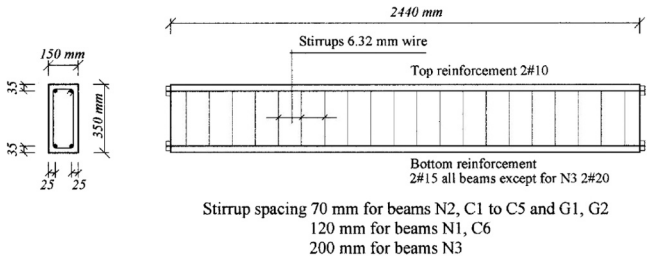

Fig. 49. Beam sketches and loading system [43].

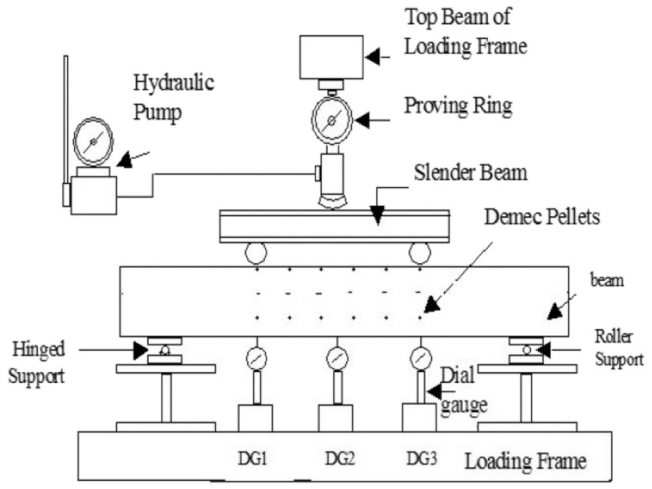

Fig. 50. Beam test setup schematic drawing [43].

4.12. Ghobarah et al. (2012) [43]

Fig. 49 demonstrates the beam sketches and loading system, while Fig. 50 illustrates the beam test setup schematic drawing. Internally bonded strain gauge was the main instrument for beam testing. The beam surface was attached with a strain gauge before it was reinforced with steel or FRP. In addition, the strain gauge was attached to the centre and one-third of the beam span from the supports. Demec gauge was additionally applied to the flanges and web parts at the centre and one-third from the load distance to measure linear stresses gained from the beam testing. Vertical deflections from one-third of load locations were measured using LVDT. For static load, the load increase was maintained at 3 kN/sec until beam failure occurred. At regular intervals, the crack width was investigated using microscopes to magnify the cracks' propagation on the beam surface before the beam failed.

CFRP and GFRP bars of 15 mm in diameter length were utilised to create the beam anchors. The CFRP and GFRP anchored bars influenced the structural beam performance by raising the load capacity by 76% and 80%. After peak stress, GFRP and CFRP strengthened beams in both anchored and non-anchored systems failed in shear and flexure. Without a stirrup inside the crucial shear span, the ultimate load-bearing capability of a shear-strengthened beam made from mechanically attached hybrid FRP improved by 83%. Nevertheless, the identical strengthening method resulted in a 70% increase in beam strength equipped with an interior steel stirrup. Beams reinforced with FRP wrapped at 45° had high resistance to diagonal fracture development than beams reinforced with FRP wrapped at 0^0 and 90°. After experiencing maximum load, the shear fractures in FRP-strengthened beams propagated downwards with a uniform diagonal arrangement. The majority of shear-strengthening designs assumed that shear cracks would form at a 55° angle, but some studies of shear-strengthened beams illustrated that this angle ranged from 40° to 70°, depending on the shear and flexural strength parameters of the FRP system. Increasing the U-wrapped FRP area by 34% led to an 18% increase in load capacity.

For continued ductility and sufficient shear capacity, including intermediate anchoring of FRP laminates in any U or V wrapping system with flexural strengthening reinforcement could be carried out on the beam performance. The shear strength of anchored and unanchored beams was improved using EB FRP. This finding demonstrated that EB FRP was in parallel contact with the internal steel stirrup. Some models were used to provide appropriate design parameters for shear strengthening, incorporating the unfavourable link between the internal stirrup and EB FRP. A strong steel stirrup inside the beam component hinders the use of EB FRP capacity. The inner steel stirrup could not be transected by the crucial shear fractures, preventing the beams from reaching their ultimate state limit. The FRP wrapping direction determined the reinforced beams' cracking pattern propagation.

Before designing the shear strengthening system, it was vital to analyse the cracking pattern dimension, size, and shape because all these factors were essential to determine how they would affect the FRP beam design strength and failure characteristics. Besides that, increasing the input property by expanding the area covered by FRP had the potential to increase the output acquired. Mounted FRP strips using NSM method also significantly improved the shear strength by increasing the bond interface area relative to the strip cross-sectional area. Many factors influenced the installation effectiveness of the NSM-strengthening system, such as layer number of FRP strip, FRP wrapping method, steel reinforcement type, concrete cover thickness and strength. The successfulness of the FRP strengthening method was demonstrated by the beam transition failure from brittle shear to ductile flexural at ultimate stress. Utilising FRP U-wrapped method in RC beam changed the beam failure mode from brittle shear to ductile. In conclusion, it was essential to keep in mind that FRP had many benefits to the structural improvement of RCB.

4.13. Effect of temperature on fibre reinforced polymer reinforced concrete beams

29 RCB were subjected to experimental testing to study the effect of heat levels (30, 300, 500, and 700 ^{0}C) on the behaviour of FRPRCB [44]. When reinforced with FRP, the percentage dropped to 3–27% but went up to 7–33% when exposed to higher temperatures. In contrast, raising the temperature had the opposite effect in increasing strain levels. Doubling the temperature values resulted in greater yielding stiffness compared to initial stiffness. Heat levels of 30, 300, 500, and 700 °C were the experimentally tested factors that were considered on the stiffness behaviour of 65 RCB [45]. According to the experimental results, the elastic and yielding stiffness decreased with increasing temperatures. However, raising the temperature values twice as high as those reported for the yielding stiffness greatly impacted initial stiffness. This research study investigated the flexural behaviour of RCB strengthened with various configurations of FRP exposed to 28 ^{0}C room temperature and 65°C hot water for three years [49]. The environmental factors didn't affect the bond strength between FRP and concrete tension side. This meant that no separation or debonding occurred. The RCB failed under compression when the load caused inelastic deformation in concrete, causing the yielding of primary steel reinforcement. RCB reinforced with FRP showed improvements in ductility and decreased flexural stiffness. There was also a 0.9% drop in average ultimate load for every 1.5% drop in concrete compressive strength due to heat contamination [51]. The average RCB toughness decreased by 13%, 22%, and 48% at 160 ^{0}C, 260 ^{0}C, and 500 ^{0}C. The higher the FRP sheet layer and temperature, the lower the average RCB toughness. Exposure to high temperatures of 300, 500, and 700 ^{0}C caused the RCB to fracture extensively, reducing their stiffness, ultimate deflection, ductility, and yield deflection by 9–33%, 35–76%, 20–51%, and 7–52%, respectively [52]. At temperatures below 160 ^{0}C, the mechanical and structural behaviour of RCB were significantly affected, as evidenced by the low shear force produced, whilst at temperatures over 260 ^{0}C, the effect was

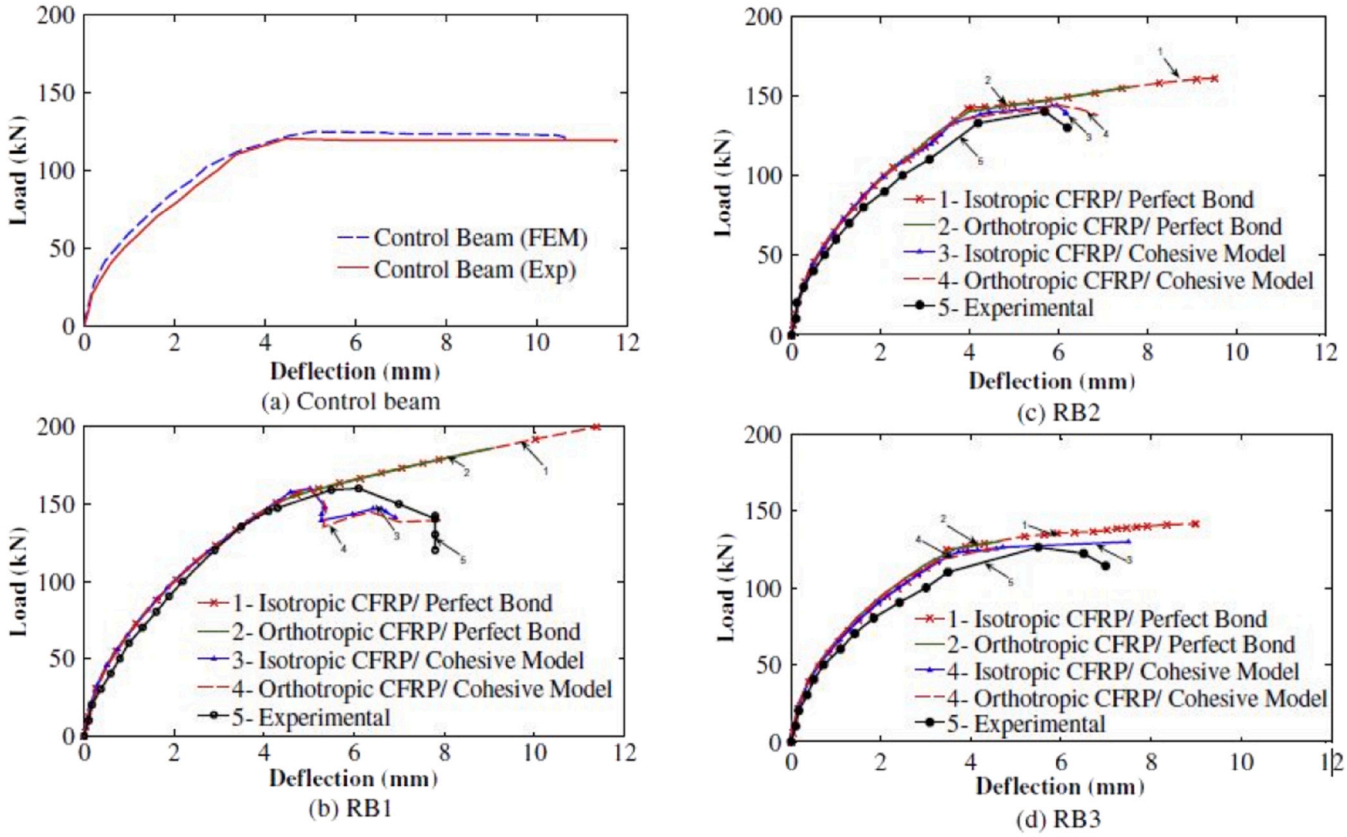

Fig. 51. Load-deflection [71].

more notable, causing the concrete to fracture extensively without spalling [53]. Reducing flexural and shear capacities at temperatures below 160 ^{0}C and increasing stiffness beyond 260 ^{0}C were the two most noticeable effects of thermal shock on the structural behaviour of RCB, causing the crack propagation on the RCB surface to expand and wider before failure occurred [54,55]. Reinforcing the slab samples with CFRP laminates drastically reduced their capacity by 7% [62]. Typically, doubling the exposed temperature resulted in 9% decreased, which might be further enhanced by raising the temperature over 600 ^{0}C. Moreover, the declining percentage rose from 7% to 43% when exposed to high temperatures but fell to 3–37% as the concrete strength increased.

4.14. Effect of sulphate on fibre reinforced polymer reinforced concrete beams

No separation or debonding was seen in the tested bond strength between FRP and concrete tension side, indicating that environmental conditions had no impact on this bond created [49]. The concrete exhibited inelastic deformation upon loading, which caused the primary steel reinforcement to yield and the tested RCB to fail under compression mode. Also, the RCB's ductility improved, but the flexural stiffness deteriorated. The FRP enhanced the RCB's ultimate shear strength, ductility, and stiffness, as the experimental tests proved. The experimental results also depicted that the RCB might have reduced their crack width by being reinforced with FRP composite materials [57]. The energy absorption value declined as the sulphate attack rose. In addition, various opening ratios resulted in a decrease in the energy capacity ratio [62]. The opening ratio was also linearly related to the energy capacity ratio. On the other hand, the RCB's elastic stiffness diminished by 10%, 11%, and 19%, respectively, as the sulphate attack increased [63]. Apart from that, the ductility capacity produced 12%, 30%, and 60% energy absorptions less than normal RCB without FRP reinforcement. The RCB performance with a small opening size (3%) was significantly improved by using PF at percentages higher than 0.7%, while the RCB performance with a big opening size (9%) was slightly improved [64]. Hence, optimising the polypropylene fibre (PF) percentage and opening size could replace the conventional steel reinforcement used in standard RCB. The effects on energy absorption, displacement, ductility index, and final deflection were highly affected by discontinuous structural synthetic fibre (DSSF) percentage and moderately influenced by FRP length [65]. Additionally, sulphate attack also impacted the RCB's yield strength, stiffness, and stress-strain but had negligible effect on ultimate strength. Furthermore, based on much prior research, DSSF had a minor effect on RCB's structural performance. Moreover, the anchoring method improved the RCB's structural behaviour and properties by making the FRP sheets more efficient. Using DSSF and FRP U-wrap configuration benefited the RCB performance by preserving their integrity before and after cracking, preventing ductile failure mode, arresting internal and external crack propagation, and improving overall structural performance concerning strength behaviour and serviceability performance [66]. Decreased hysteresis loops, ductility, and more stiffness deterioration were the typical outcomes of RCB's performance when exposed to sulphate attack [67]. Besides that, the joint stress was reduced, and the steel yield was distributed narrower than standard RCB using typical steel bars. The bond-slip behaviour between FRP and RCB was greatly influenced by the use of DSSF in reinforced concrete [68]. It was found that adding 0.44% and 0.66% of DSSF to the concrete mixture improved the bond force by four to seven times compared to normal RCB with 0% DSSF. Similarly, the corresponding slip increased by approximately 2–3 times more than conventional RCB with 0% DSSF. The FRPRCB reached a bigger displacement upon failure because the applied load on the FRPRCB was uniformly distributed [69]. The energy absorption grew substantially with increasing fibre volume

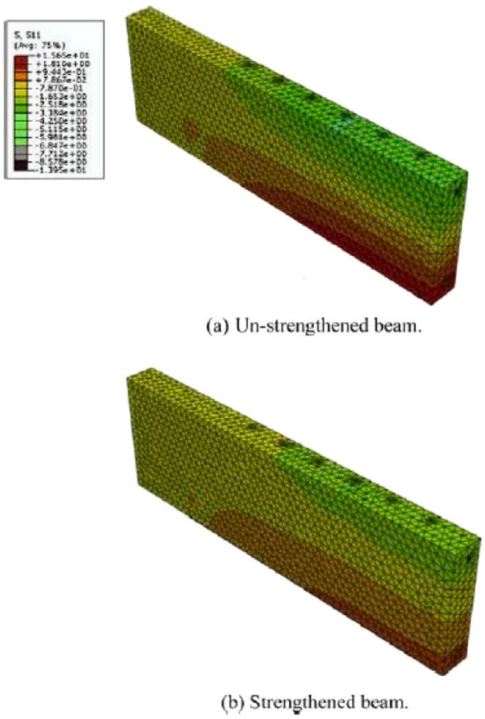

(a) Un-strengthened beam.

(b) Strengthened beam.

Fig. 52. Axial stress (RB2) [71].

(Vf) [70]. The FRPRCB with 0.6% and 0.88% Vf absorbed around 3.8–4.8 times more energy than the FRPRCB with 0.44% Vf, respectively [44–70].

5. Finite element analysis of fibre reinforced polymer reinforced concrete beams

The results of numerical modelling on the structural efficiency of fibre reinforced polymer reinforced concrete beams (FRPRCB) are reviewed in this section.

5.1. (Obaidat, 2022) [71]

This research aimed to learn and deeply investigate the structural behaviour of RCB strengthened with FRP composite material. Beams that were aimed to fail in flexural or shear were the primary targeted failure in this NM. The cracks appeared and propagated on the beam surface after being tested under four-point bending test. After that, the beams were unloaded, followed by FRP installation on the exterior surface of the beams. The last step was to investigate the beams until they failed. The NM was developed using ABAQUS software to simulate the beams' structural performance. The beams' load-deflection behaviour until failure, failure mechanisms, and crack patterns were compared with analytical findings from the experimental data. Afterwards, the finite element models (FEM) were employed to examine the effects of various factors on the behaviour of retrofitted beams with FRP composite material and also to determine the optimal composition of FRP to achieve the highest increased in load capacity.

After seven months of air curing, thirteen beams were subjected to four-point bending tests consisting of two beam sets. The shear and flexural behaviour was the main emphasis for groups RS and RF. Two beams were denoted as control beams for group RF. Before being retrofitted with FRP, the remaining six beams were preloaded before being retrofitted with FRP until flexural fractures were detected. Two beams of almost similar span was utilised for each of the three groups of FRP beams. All control and FRP beams were subjected to two-point loads until failure occurred. Two beams served as control in group RS, while

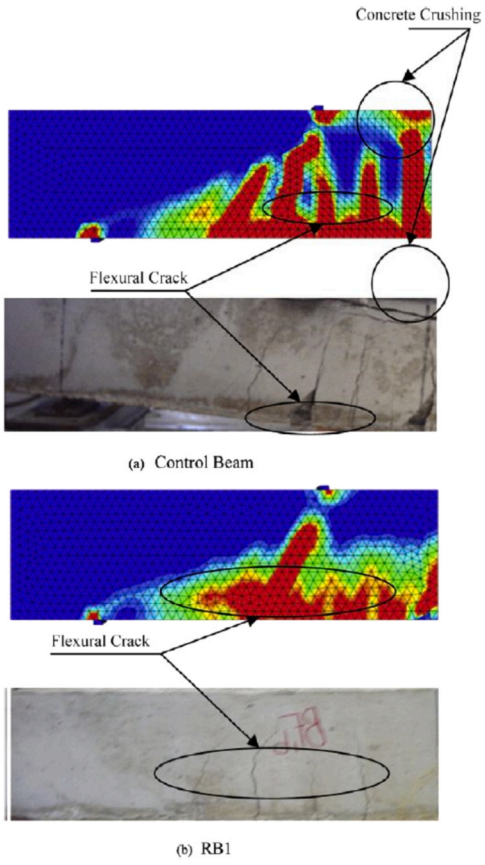

Fig. 53. Plastic strain [71].

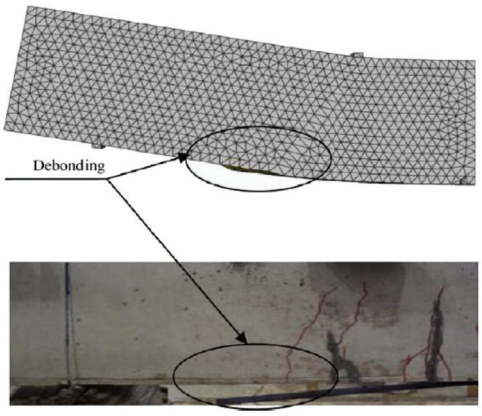

Fig. 54. Failure mode [71].

the remaining two beams were subjected to preloading until shear fractures emerged after they were retrofitted with FRP and tested until they failed.

The load-deflection curves for the control and retrofitted beams by experimental and NM are shown in Fig. 34. Two distinct experimental configurations were used: FRP and concrete/FRP bonding models. A good agreement was found between NM and experimental results for the control beam depicted in Fig. 51(a). It was evident that the FRP length had a major effect on the beam's structural behaviour, as displayed in Fig. 51(a)-(d). The longer the FRP length, the higher the maximum load obtained. Fig. 51(b)-(d) illustrate that all four NM models for the retrofitted beams produced comparable findings and were stiffer than experimental data throughout the initial section of the curve. Fig. 52 (a) and (b) show the axial stress under a load of 11 kN for the control and

FRP retrofitted beam specimens. Fig. 53(a) and (b) compare the plastic strain distributions and fracture patterns between the experimental study and NM for control and FRP-strengthened beams. Fig. 54 illustrates that the debonding fracture used the same cohesive bond model as in the experimental study.

Due to the predicted complete connection between concrete and reinforcement, the beam was anticipated to be stiffer and stronger than the NM findings indicated. The constitutive models often employed in concrete and reinforcement successfully reflected the beam's fracture behaviour because of the high degree of concordance. As cracks occurred, the beam's stiffness decreased while the shear strain increased. Perfect bond models persistently overestimated the beam's stiffness after the fractures emerged. The perfect bond disregarded the shear strain acquired between concrete and FRP. For RB1, the beam softening was more pronounced and the ideal bond models did not successfully capture it. The perfect bond hypothesis could not explain the experimentally observed debonding failure. The load continuing rose until a new failure mode was achieved. There was either an FRP rupture or a shear-flexural fracture failure. Isotropic and orthotropic perfect bond models generated comparable curves. The orthotropic model projected the maximum load to be modest. The isotropic FRP was confined to such a high degree of strength, causing it to become abnormally stiff in transverse and shear directions. Cohesive models were found to be in reasonable accord with experimental results. Similar results were found in both isotropic and orthotropic cohesive models. The cohesive model was shown to be in good agreement with the test conducted, whereas the perfect bond model was in poor agreement with experimental results only for big weights imposed. Several potential causes exist for the disparities between the experiment and NM findings. One of the potential causes was the control beam's concrete and steel reinforcing formed a seamless unit. The mismatch between the experimental and NM data regarding the pre-position cracks and sizes might have been due to the predicted behaviour of the interface between FRP and concrete. The element's stiffness and capacity could be exaggerated as a result. Subsequently, the NM results showed that the orthotropic properties of the unidirectional FRP could be neglected.

Compared to the normal beam without FRP, this NM demonstrated that the FRP strengthening had systemic implications on the beam's stress distribution. The stress distribution of the FRP-strengthened beam also greatly differed from the unreinforced beam, which did not have FRP retrofitting. All models, including this NM, corroborated the experimental results. Initial crack propagation foci was the greatest positive primary plastic strain site. The material integration point was thought to be the starting point of crack propagation. The similarities between the fractures observed from the experimental and NM findings concluded that the NM reflect the fracture mechanics of the beam. The ideal bond model did not predict the debonding fracture mode in this study since it did not meet the essential criteria for bond breaking. However, a cohesive model could be used to simulate the debonding.

Various failure modes could arise in FRP based on NM simulations. These NM were depended on the beam's geometry and stiffness. Debonding was a common failure condition caused by stress concentration in the zone between concrete and FRP. Accordingly, minimising stress concentrations was crucial in FRP retrofitting design steps. A significant stress concentration will occur at the end plate if the FRP is highly stiffer and narrower. Furthermore, FRP debonding occurred before steel yielding, causing the beam to fail at a low load imposed. Thus, it was best to prevent this from happening at all costs. For a given stiffness, a wider FRP plate will always result in a larger maximum load, but increasing the FRP plate stiffness will raise the maximum load to a specific value and then drop to an optimal value.

5.2. (Song et al., 2022) [72]

This research aimed to comprehend the mechanical inelastic behaviour of steel-concrete composite beams reinforced with FRP laminates under negative moments. The NM with the layout width of FRP laminates equal to 200–700 mm, respectively. This research was conducted to analyse the impact of FRP layout width on the mechanical properties of composite beams in negative moment regions with the composite beams' structural size assumption. Monotonic load tests were conducted on a simply supported plain beam and continuous FRP composite beams in order to observe and compare the negative moment results produced. The experimental test results were used to validate the ANSYS NM, yielding several mechanical parameters like load-deflection and stress-strain curves. The control NM beam was used as the foundation model, while the additional NM beams were reinforced with FRP laminates. The mechanical characteristics of composite beams with and without CFRP laminates were subjected to negative moments. All the beams' mechanical behaviour were investigated and compared with each other. Furthermore, parametric analysis was utilised to find out how bearing capability was affected by CFRP layout width and length, layer number, longitudinal reinforcement ratio, and shear connection types. Its intended purpose was to focus, help, and serve as a guide for engineers, scientists, researchers, and academicians working on real-world construction projects involving these kinds of FRP composite beams.

Table 12
NM results [72].

Width (mm)	Crack load (kN)	Yield load (kN)	Ultimate load (kN)	Final crack load (kN)
100	68	898	1116	63
200	70	906	1220	63
300	70	906	1249	64
400	70	913	1257	64
500	70	919	1261	64

The beam specimens had a computed span of 3.5 m and a total longitudinal length of 4 m. The beam stood up at 600 mm in height, composing 360 mm I-beam, 160 mm concrete thickness, and 700 mm wide with C40 concrete grade. The beams incorporated Y-500 hot-rolled ribbed steel bars with 17 mm length and 11 mm width. Moreover, the longitudinal reinforcing bars had a ratio of 5%. All web, top, and bottom flanges had 13 mm, 14 mm, and 15 mm thicknesses, respectively, while the entire steel beam used R40 steel grade.

Table 12 compares the composite beams' ultimate, yield, and cracking loads with varied laminate widths. It used 5:6:2 reinforcement ratio. The FRP beams' reinforcing bar yield load grew by less than 6% compared to conventional beams without FRP laminates when the reinforcement ratio was high and the growth rate reached 19% when the reinforcement ratio was low. Furthermore, as observed in Fig. 55(a), the load of the reinforcing bar in the beam with FRP laminates at yield stage rose by less than 13% when the reinforcement ratio was low. The ultimate load increased linearly with increasing crack pattern size when the reinforcement-to-growth ratio was only 26%, as displayed in Fig. 55(b). Running an FEA model that accounted for the arrangement location (Fig. 56) allowed us to examine the bearing performance of composite beams and identify the impact of unbonded concrete beams in a negative moment area. The FEA model established a 0.6% longitudinal reinforcement ratio for the concrete beam and a 300 mm width for the FRP beam. Fig. 57(a) illustrates that, as expected by the standard computations, the load-deflection curves of the composite beams with different FRP laminate arrangement locations were quite similar. Fig. 57(b) demonstrates the maximum tensile stress curves as a function of load for FRP laminates. Before the concrete fractured, the maximum tensile stress of the FRP laminates was quite close among the three arrangements. Table 13 displays the composite beams' ultimate, yield and cracking loads constructed from the FRP laminate layer numbers. Based on the experimental findings, bonding FRP laminates in a beam could raise the cracking load by around 6%. The load-bearing capability of the composite beam did not noticeably improve with the increase in the

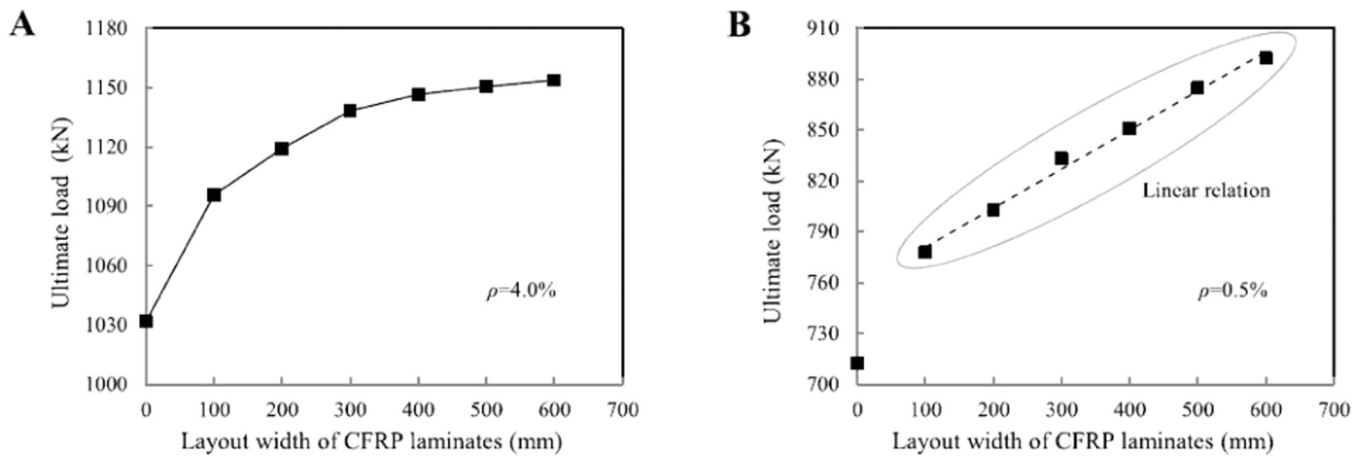

Curve of the ultimate load varied with CFRP width: **(A)** reinforcement ratio ρ = 4.0%; **(B)** reinforcement ratio ρ = 0.5%.

Fig. 55. Ultimate load-FRP width [72].

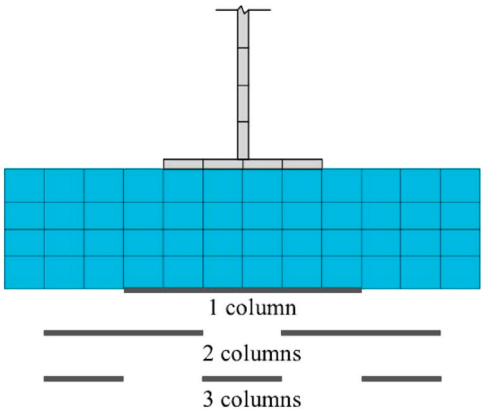

Fig. 56. FRP arrangement [72].

number of bonded layers (Fig. 58(a)). There were no discernible correlations between the number of adhesive layers and the load-bearing capacity (Fig. 58(b)).

Increasing the number of FRP adhesive layers was a standard engineering practice for guaranteeing the beam's load-bearing capacity. However, this method sometimes threw away some useful resources in its conservatism. The influence of FRP laminate layer number on mechanical characteristics of composite beams with 1–6 FRP laminate layers was studied using calculation by numerical modelling method. The three rows of FRP laminates each measured 700 mm in width. Nonetheless, adding more FRP layers did not result in any appreciable gains. The composite beam joined with FRP laminates enhanced the load at yield stage by less than 11% when the reinforcement ratio was high compared to the beam without FRP laminates. Reducing the reinforcing ratio improved the bearing performance of the composite beams, consisting of 1–4 layers of FRP laminates. The yield and ultimate loads of the reinforcing bar increased by 27% and 31% when the beam was reinforced with four layers of FRP laminates. Combining real engineering

Table 13
NM results [72].

FRP layer (mm)	Crack load (kN)	Yield load (kN)	Ultimate load (kN)	Final crack load (kN)
0	68	877	1142	61
1	70	924	1135	64
2	70	939	1253	64
3	70	930	1271	64
4	70	955	1287	64

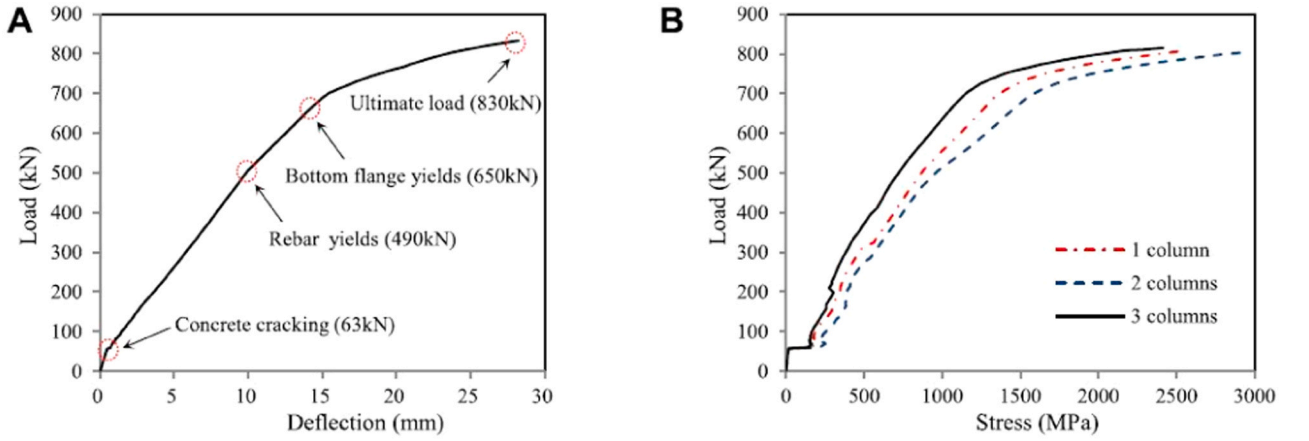

Variation curves of deflection and CFRP stress: **(A)** load-deflection curve; **(B)** load-maximum tensile stress of the CFRP curve.

Fig. 57. Load-stress [72].

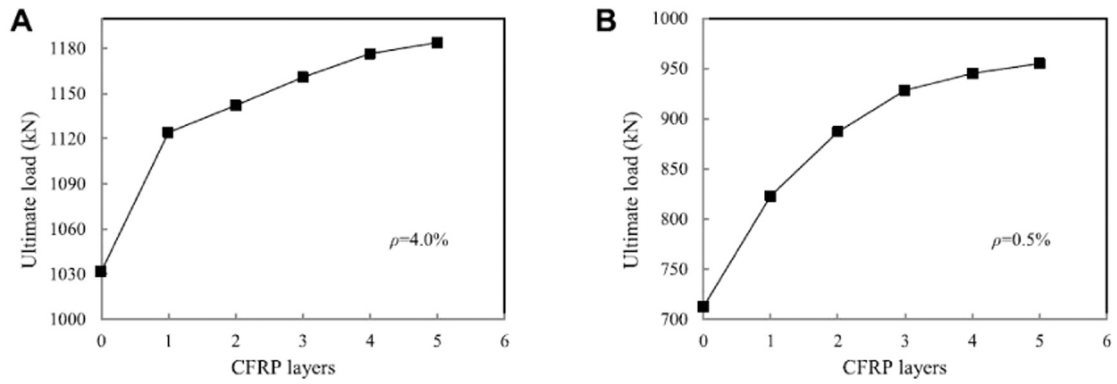

Curve of the ultimate load of the composite beam varied with CFRP layers: **(A)** reinforcement ratio ρ = 4.0%; **(B)** reinforcement ratio ρ = 0.5%.

Fig. 58. Ultimate load-FRP layers [72].

factors, such as FRP layer numbers, with design limitations through experimental study and numerical modelling was crucial before analysing the results obtained.

The NM reliably predicted their general mechanical behaviour when negative moments were applied to steel-concrete composite beams. Taking the interface slip effect on NM calculations brought their findings closer to experimental values. The primary reason why NM had bigger non-linear stiffness than the actual data was because it assumed a perfect connection between FRP reinforcement and concrete bond connections. It also ignored the weak influence of shear connectors in FRPRCB. Furthermore, the composite beams' load-bearing performance was unaffected by changing the FRP laminate layout position as the overall width of the FRP laminates remained constant and permanent based on FRP layout position analysis effects. The maximum tensile stresses of FRP laminate arrangement using various layouts were nearly constant prior to concrete cracking and debonding. Nevertheless, the maximum stresses of FRP laminates stacked in three columns were less than the other two beams after the cracks emerged on the beam surface.

5.3. Barbato (2019) [73]

They created a novel non-linear NM that relied on the typical Euler-Bernoulli formula equation to simulate the structural performance of RCB reinforced with FRP. In the sequel, this NM simulated and analysed the FRPRCB behaviour. It had three primary purposes: (1) to simplify and reduce the computational cost of the latest NM using existing FE models; (2) to explain and discuss intensely what would happen when FRP-retrofitted RC beams failed at the end; and (3) to accurately simulate the structural response and integrity of FRPRCB's consideration system, making it suitable for industrial demand and real-world construction projects.

The existing element, section, and 29 materials were expanded using ANSYS's modularity to allow for accurate NM and simulation of RCB structures with flexural strengthened members by externally bonded FRP plates. These extensions included a 7-VOI displacement-based RCB element with 30 FRP shear and flexural reinforcements, 7-VOI force-based RCb element with 31 FRP shear and flexural reinforcements, beam cross-section with FRP reinforcement included debonding, and new cyclic FRP material model included debonding. In addition, these NM might be readily expanded to include more sophisticated models for debonding. The NM's initial state was considered as a slip bond between FRP reinforcement and concrete in order to represent the current state of structural modelling. In particular, NM for RCB structural behaviour was performed to create a non-linear frame element to simulate and analyse the beam shear performance and column confinement retrofitted with FRP plates.

Fig. 59 depicts the geometric parameters of the specimens as

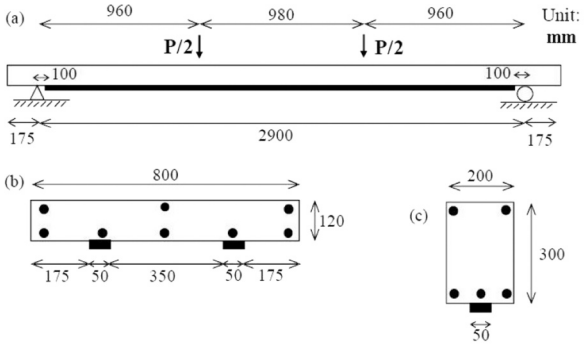

Geometric properties of the specimens tested for both slab and beam specimens, (b) cross-section geometry of the slab specimens, and (c) cross-section geometry of the beam specimens : (a) shear span and loading condition

Fig. 59. Beam geometrics [73].

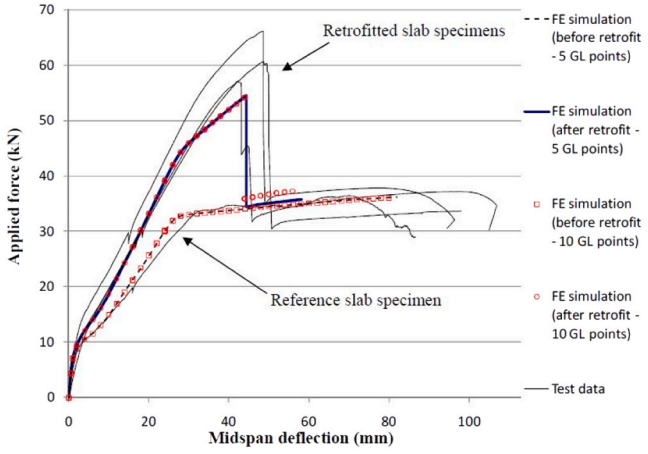

Fig. 60. Applied force-mid span deflection [73].

evaluated in 4-point bending test. Three reference beams and three similarly constructed FRP-retrofitted beams had their own reactions to the applied load at midspan, as depicted in Fig. 60. Proper FE simulation of the beam reaction required detailed modelling analysis for the FRP reinforcement arrangement, which was attached to the beam soffit as two independent FRP sheets (Fig. 59(b)). These findings were derived by utilising the geometric parameters of a single FRP sheet applied to 1/2 of the beam cross-section. Two parameter values were used: bc = 500 mm

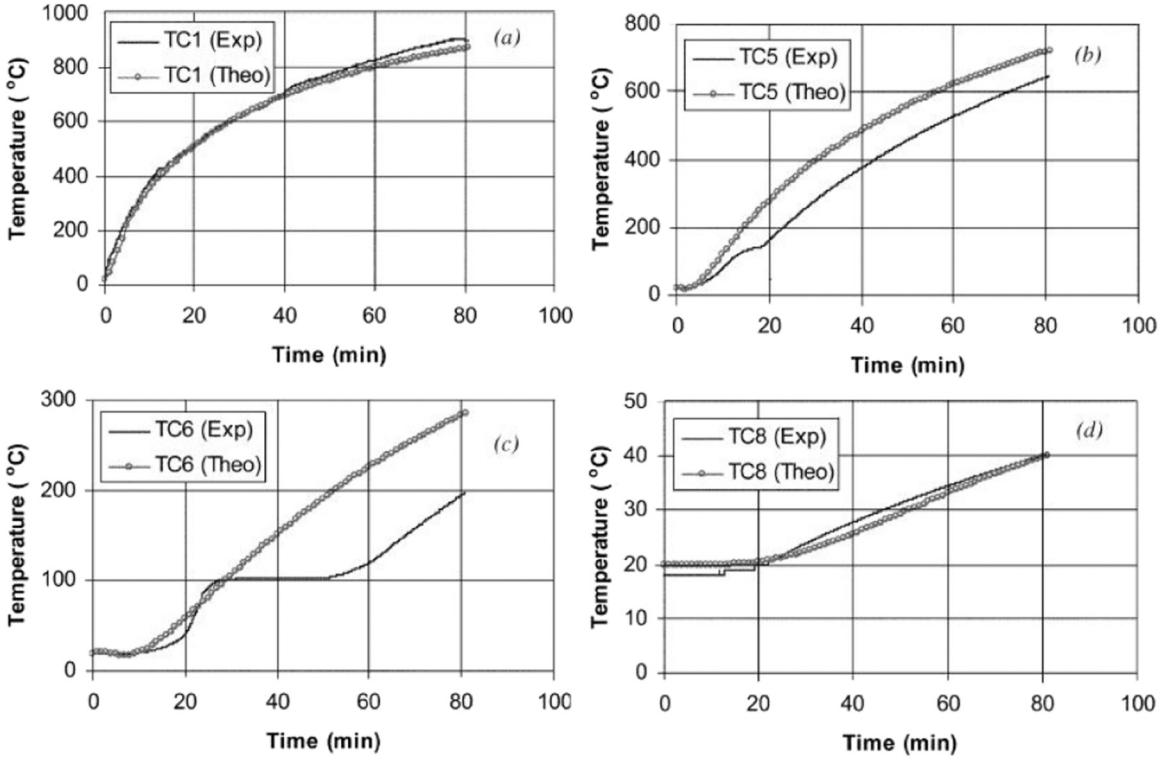

Fig. 61. Temperature-time [74].

and bf = 60 mm. The FE simulation used bf and bc values to determine the beam load-carrying force capacity (Pu) and mid-span deflection (L) of 55 kN and 45 mm. According to FE simulation data results, the Pu and L declined to 51 kN and 38 mm because the beam design strength was reduced to 8%, but the configuration of the FRP reinforcement was maintained.

Through empirical and numerical simulation, this research compared the reference and FRP-retrofitted beams' responses to the applied load at their mid-span. Few studies in the database also included the tested specimens' reactions. The FRP-retrofitted and reference beams were distinguished by marking the beam surface. A circle mark was made on the FRP-retrofitted beam surface, while a square mark was made on the reference beam surface. These marks provided the finite element (FE) response simulation for FE meshes constructed with two FE having 20 intersection points each. So the total intersection points for two FE were 40. At the same time, the thin solid lines corresponded to the experimental results by having a value of n=40. Both numerical simulation and experimental data for reference and FRP-retrofitted beams agreed well. Besides that, the findings from the two FE meshes with five and ten GL integration points were almost coincident, proving that using five intersection points was adequate to guarantee the results' objectivity before the peak strength was attained. The FE simulation underestimated the shear and ductility of the FRP10 retrofitted beam. Still, its initial stiffness, concrete cracking under stress, concrete cracking under tension, and post-peak stiffness corresponded well. However, the FRP-FB13 beam element did not have any technique to ensure the modelling objectivity for softening the beam's structural behaviour. No attempt was made to estimate the ductility, followed by the steel yielding under tension force.

In conclusion, this NM stood out for its straightforward design and effective mesh refining. The NM was designed and executed using beam cross-section discretization in layers to produce an excellent structural reaction between axial and bending behaviour automatically. Moreover, all constitutive models of non-linear FRP materials had been designed and implemented to support dynamic and cyclic quasi-static analysis. Furthermore, parametric studies on various retrofitting configurations could be quickly and correctly conducted using these NM steps and methods. It was also appropriated for modelling and analysing flexural strengthening of reinforced concrete column, slab, and frame structures utilising 40 FRP plates or sheets. As a result, research on extending the planned FRP retrofitted beams with two frame members and high shear strength was ongoing.

5.4. Rafi et al. (2018) [74]

The experimentally recorded beam structural behaviour was used to validate the NM analysis to determine how concrete and steel's thermal expansion coefficients changed when heated to high temperatures. Besides that, the suggested relations were applied to commercial NM software to do the FEA calculations in accordance with the smeared crack (SC) ideas. There were several notations used for the beam NM, such as B for beam, R for 28 ^{0}C room temperature or rising temperature, and S for specified material types for strengthened compression and tension forces of reinforcing bars, either steel or FRP composite material. For instance, the first of the two beams was strengthened with FRP bars and heated at high temperature, denoted as CEB1.

This study detailed an NM, contrasting the experimental and NM beam behaviour at high temperatures. Beams reinforced with FRP and regular steel bars had a 130 ×210 mm cross-section. The beam's overall length was 2100 mm with 1800 mm span, including 25 mm concrete pavement depth. The FRP rods' diameter was 10 mm with 1700 MPa and 136 GPa load strengths. The FRP bar type utilised was high-strength deformed steel with 11 mm diameter with 540 MPa steel strength (fy) and 202 GPa modulus of elasticity (Es). On the other hand, a set of similar closed square stirrups with 7 mm diameter and 110 mm center-to-center spacing was supplied. Then, the beams were subjected to four-point static load test with two end supports. The load span had 410 mm spacing and it was applied at 41% of the ultimate capacity.

Beam BES1 lasted the longest. Several places of BES1 had their analytical temperature profiles drawn out, as shown in Fig. 61. The

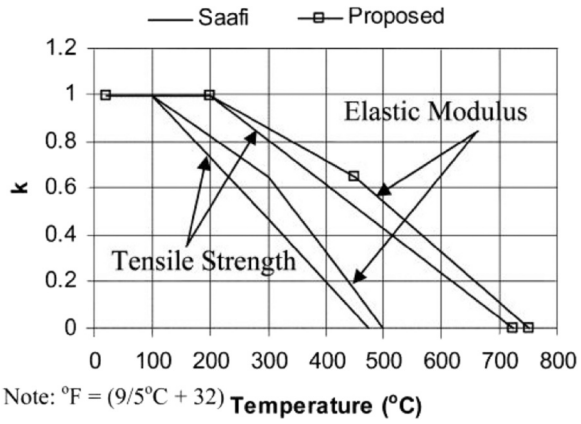

Fig. 62. K-temperature [74].

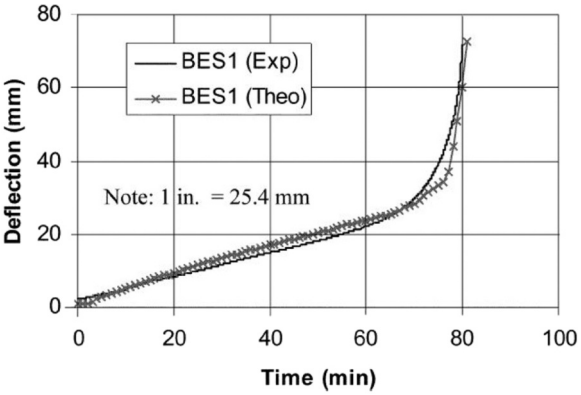

Fig. 63. Deflection-time [74].

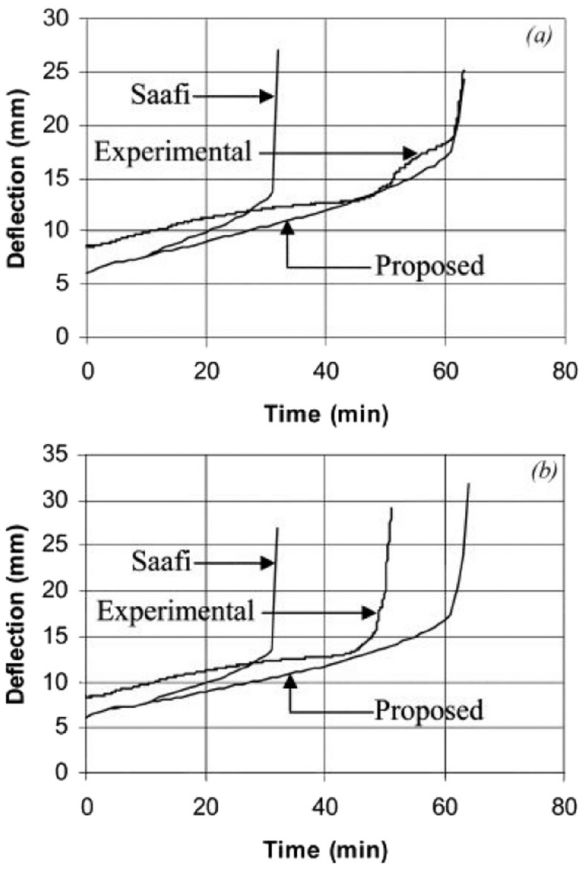

Fig. 64. Deflection-time (a) BEC1 (b) BEC2 [74].

projected and measured temperatures were well relatively connected within the time-temperature relationship. After 100 °C, the analytical curves deviated from the recorded data in Fig. 61(b) and (c) because water evaporated. The effects of moisture evaporation were the most prominent at the most distant fibres from the heating surfaces, leading to an overestimation of temperature value in the heat thermal analysis (Fig. 61(c)). Saafi 30 model (Fig. 62) was used to predict how the characteristics and properties of FRP bars would change or not, as well as the changing of the temperature. Fig. 63 delineates a contrast between the experimentally observed and theoretically expected beam mid-span deflection as a function of heating time. The prediction function of heating time was calculated and compared using the BEC beam deflection in Fig. 64. The model overestimated the strength of BEC2, as demonstrated in Fig. 47(b). Fig. 64 clearly demonstrates that both beams' anticipated failure periods were consistent and preserved, supporting the theoretical behaviour comparison results for BEC beams.

Thus, its temperature was measured and compared to the maximum theoretical value. The beam's virtual mesh was chosen to illustrate the thermocouple sites as discrete points. The mesh size and the boundary layer of the heat transfer coefficient significantly impacted the predicted temperature distribution. This evaporation was a physical process that was not considered in the numerical simulation. Nevertheless, the two curves were parallelly connected to one another. The anticipated and observed deflections at each beam heating step showed a reasonable correlation degree relationship. The projected deflection was turned down between 20 and 70 boiling minutes. During this time period, the anticipated bar temperatures were bigger than the measured temperatures. The simulation model extremely predicted conservative beam behaviour. There was a clear need to get a more precise relationship between the temperature and the mechanical characteristics of the FRP bars. This investigation utilised an empirical strategy built based on the principle of trial and error. This procedure was repeated several times to get an accurate empirical strategy. If the lower and upper-temperature limitations were known, linear interpolation could be used to determine the FRP characteristics at various temperatures imposed on the beam surface. The expected tilt was calculated and acquired following the standard equation suggestion. In conclusion, the beams' initial stiffness at ambient temperature was underestimated due to the discrepancy between the projected and measured values of early mid-span deflection. This performance was consistent with the BRC beams as described. However, with the time passage during heating, the theoretical and experimental deflections grew relatively close and well agreed between the anticipated and observed deflections towards the beam failures. An early failure of this beam was observed during experimental testing. The uneven distribution of loads to the FRP reinforcing bars due to non-uniform deformation was the factor of the beam failure. Another factor was discrepancies in the beams' anchoring length located at the beams' end zone. A disparity in concrete strength caused BEC2 beam to collapse before matured time.

The results from the analytical temperature propagation agreed well with the data obtained from the NM analysis. Over 100 °C, the predicted and observed temperatures started to diverge because the NM did not consider and investigate the water evaporation process. The NM model gave conservative temperature predictions at a location having a high and thick layer of concrete. Both steel and FRPRCB's behaviour was accurately approximated by the smeared crack model, which was based on the concrete tangent's ductility and stiffness. The NM analysis successfully predicted the structural behaviour of standard beams and FRPRCB until failure using the temperature-dependent material for concrete, steel and FRP reinforcements.

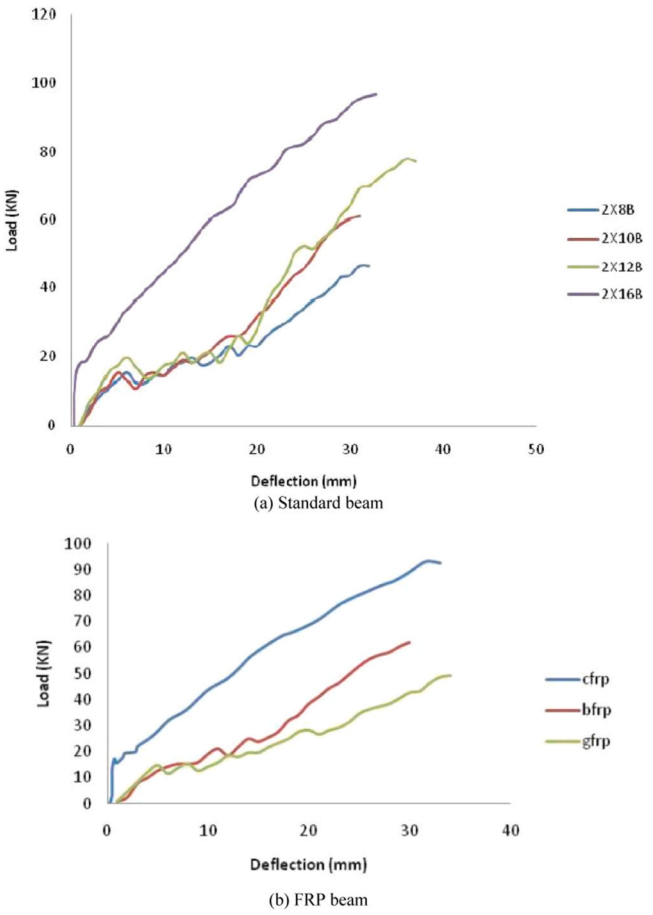

Fig. 65. Load-deflection [75].

5.5. Manish Kumar et al. (2022) [75]

The study provided a more detailed presentation of extra theoretical and NM necessary in order to understand the FRPRCB structural behaviour and performance. On the contrary, there was a current shortage of ABAQUS-based experimental investigations of FRPRCB in flexural behaviour. So, this research aimed to assess the accuracy of the NM approach in simulating the flexural load imposed on the RCB surface that had been strengthened with FRP composite material as reinforcement. This research summary will explain how to perform NM of FRPRCB by investigating the compressive behaviour of RCB reinforced with FRP bars. Apart from that, the flexural response of FRPRCB was computed, modelled and analysed using ABAQUS NM software as well. Different reinforcement ratios, including detailed FRP reinforcement, were summarised in this review finding.

As explained previously, the NM's accuracy was verified using the beam experimental results. The load-displacement graph curves for beams 3Y11C, 3Y13C, and 4Y17C were obtained by NM using ABAQUS software. All of the NM results perfectly agreed with the experimental data. Notably, the NM finding graphs consistently acquired with the previous experimental curves in most instances.

Fig. 65(a) displays the deflection as a load function for the FEM of flexural behaviour to investigate the impact of reinforcement ratio on the beam behaviour. Fracture beams with more FRP reinforcement were more robust and stiffer. Nevertheless, a strong relationship existed between the FRP reinforcement layer number and the beam stiffness inclination. The reinforcement types depicted in Fig. 65(b) affected the beams' shear and flexural behaviour. Both behaviours were improved with the inclusion of FRP. Fig. 66 shows the FE simulation result for beam 3×16 B's fracture pattern. Mises stress for beams was employed in this research study, and the findings are shown in Fig. 67(a). The mises stress was reduced for the FRP beam, as in Fig. 67(b). Fig. 67(c) displays the temporal variability of central node displacement and its relationship to caseload. Fig. 67(d) delineates the beam failure patterns.

The tested models were used in parametric analyses. The flexural behaviour of each model was evaluated after various reinforcement kinds had been included. Varying thicknesses of FRP were used to strengthen the beams. The beam properties were affected by the concrete grade used. The first fracture for all beams had the same pre-cracking rigidity. The beams would remain stiff until the first breaking force was applied on the beams' upper surface. All FRP beams had different rigidity. BFRPRCB was more rigid than GFRPRCB, while CFRPRCB was more rigid than BFRPRCB and GFRPRCB. The FRP bars' strength strongly correlated with the beam behaviour. The higher the strength of the FRP bars, the higher the beam performance. The lower the strength of the FRP bar, the lower the beam performance.

The FEM correctly map out the beam length and accurately quantify the crack propagation, despite the system's complexity. The minimum and maximum stresses occurred at the support around the loading plate. This stress formation was also identical to a beam with web reinforcing distributing tension and well supported to each other. In addition, the stress also caused arches due to bounded compression strength in the beam support. It was demonstrated that the incline rate in the beam's mid-span deflection accelerated after several repeated calculations to get a precise value. The mid-span deflection of an RCB decreased when the FRP composite material was in an elastic phase due to its high-strength bond and stiffness properties and the FRP's fibre matrix compositions. Once the FRP composite material began and entered its plastic phase, its material characteristics declined while the deflection rose rapidly as well.

The FRPRCB FEM had shown that the FRP bar diameter affected their load capacity, ductility, and stiffness. A way to improve and incline the beam's load-displacement pattern was by adding more FRP bars inside the beam as internal reinforcement, replacing steel bars. Still, even a little movement of the beams could cause the beam structure to collapse and eventually fail quickly. According to previous research, RCB reinforced with more FRP bars were more effective and efficient. From this research study, the beam's load-bearing capability inclined from 9 to 63 kN when reinforced with FRP bars compared to a typical beam reinforced with steel bars. Nonetheless, the beam's yield load was unaffected by the FRP reinforcement.

5.6. Shao et al. (2015) [76]

Additionally, this study highlighted the importance of creating a reliable FEM to investigate and analyse the cyclic behaviour of concrete-

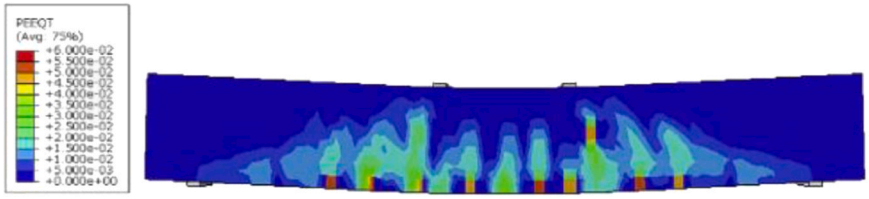

Fig. 66. Deformed shape [75].

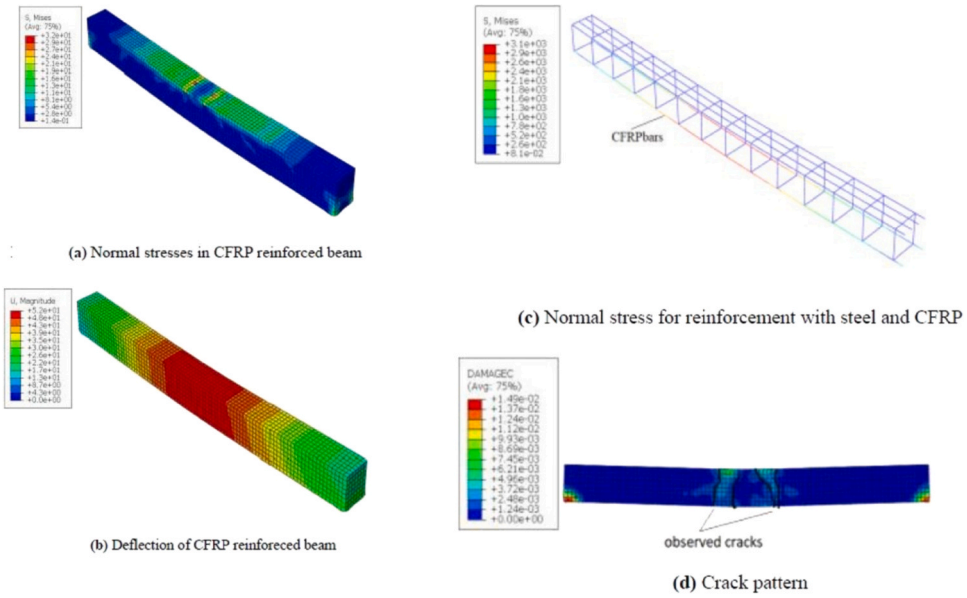

Fig. 67. Numerical modelling of FRP beam [75].

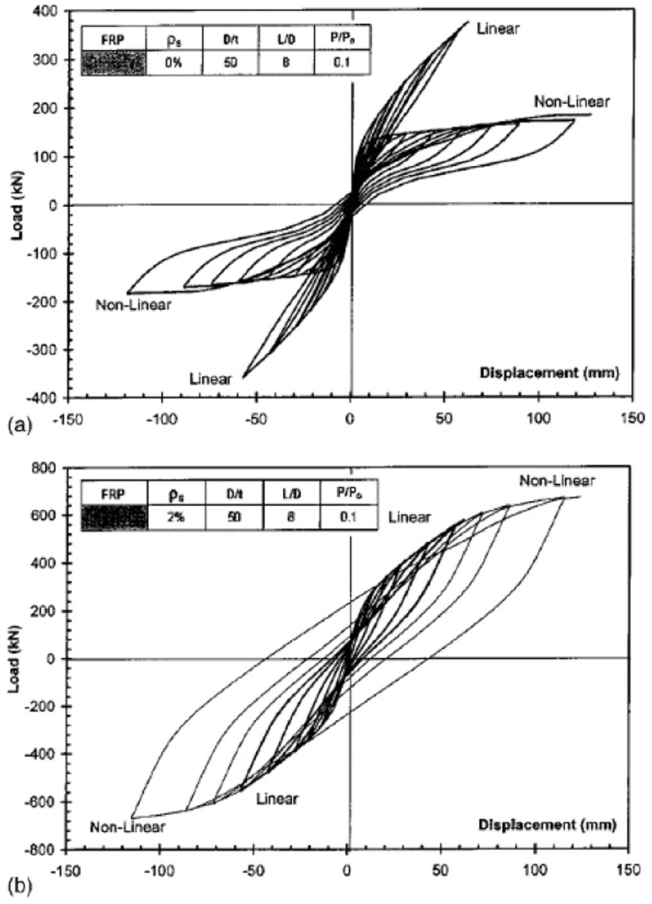

Fig. 68. Load-displacement (a) No internal steel (b) Had internal steel [76].

filled fibre-reinforced polymer tube (CFFT) beams. The CFFT beams could be represented using a detailed composite FRP element described and discussed in this review article. This FRPRCB FEM was derived from the prior work on CFST and RC filled with steel tubes. Moreover, the model was evaluated against experimental data once its components had been presented. Thus, this research was conducted to assess and observe the impact of CFFT parameters on their hysteretic response using the validated FEM. Also, the hysteretic behaviour of CFST, RC, and CFFT columns was compared to get the best FEM results.

Two cyclic reactions were observed for the FRP tubes in the coupon test. Upon unloading, there was no residual or plastic strain in the coupons made from the W series of FRP tubes, which had the most fibres running longitudinally. The failure reaction was linear. Alternatively, coupons made from a Y series of FRP tubes with ±66° fibre orientation in the laminate structure exhibited a non-linear parabolic stress-strain response accompanied by significant plastic strains when unloaded. Apart from that, previous researchers also stated that the observed non-linearity of FRP tubes was caused by interlaminar shear force.

The hysteretic response of beam-columns as a function of FRP type and internal steel reinforcement is illustrated in Fig. 68. The table in each picture section demonstrates the parameter values that were constantly maintained during the graph development shown by the grey-shaded slot. For CFFT internal steel devoid components, the effect of FRP type was more obviously proven. This FRP effect could be seen when the linear FRP offered much better capacity than non-linear FRP with significantly low energy dissipation and ductility. On the other hand, the concrete core primarily limited the capacity of CFFT with non-linear FRP. For CFFT members, the hysteretic loops of linear and non-linear FRP were combined with 3% internal steel. Nevertheless, the hysteretic loops from the non-linear FRP were larger and more stable than without FRP. Although non-linear FRP with no internal steel showed some improvements in pinching effects, non-linear FRP with internal steel still appeared to have no consequences. Non-linear FRP aided in concrete fracture closing because of its greater deformation capability. The hysteretic response of CFFT beam columns for linear and non-linear FRP with and without internal steel as a function of D/ t ratio is delineated in Figs. 69 and 70. The energy dissipation capacity and hysteretic loop were affected by the D/t ratio. The lower the D/t ratio, the higher the energy dissipation capacity and hysteretic loop and vice versa. However, it appeared that the pinching effects were unaffected by the D/t ratio. A greater D/t ratio resulted in a more flexible member. This might be because of less capacity, causing the CFFT beam-column to become more malleable due to the reduction of the tube thickness. Response pinching was often unaffected by the D/t ratio. A low L/D ratio enhanced the beam capacity and stiffness and this effect was independent of any FRP composite material or the presence of internal steel reinforcement. Also, the ductility decreased with decreasing L/D ratio

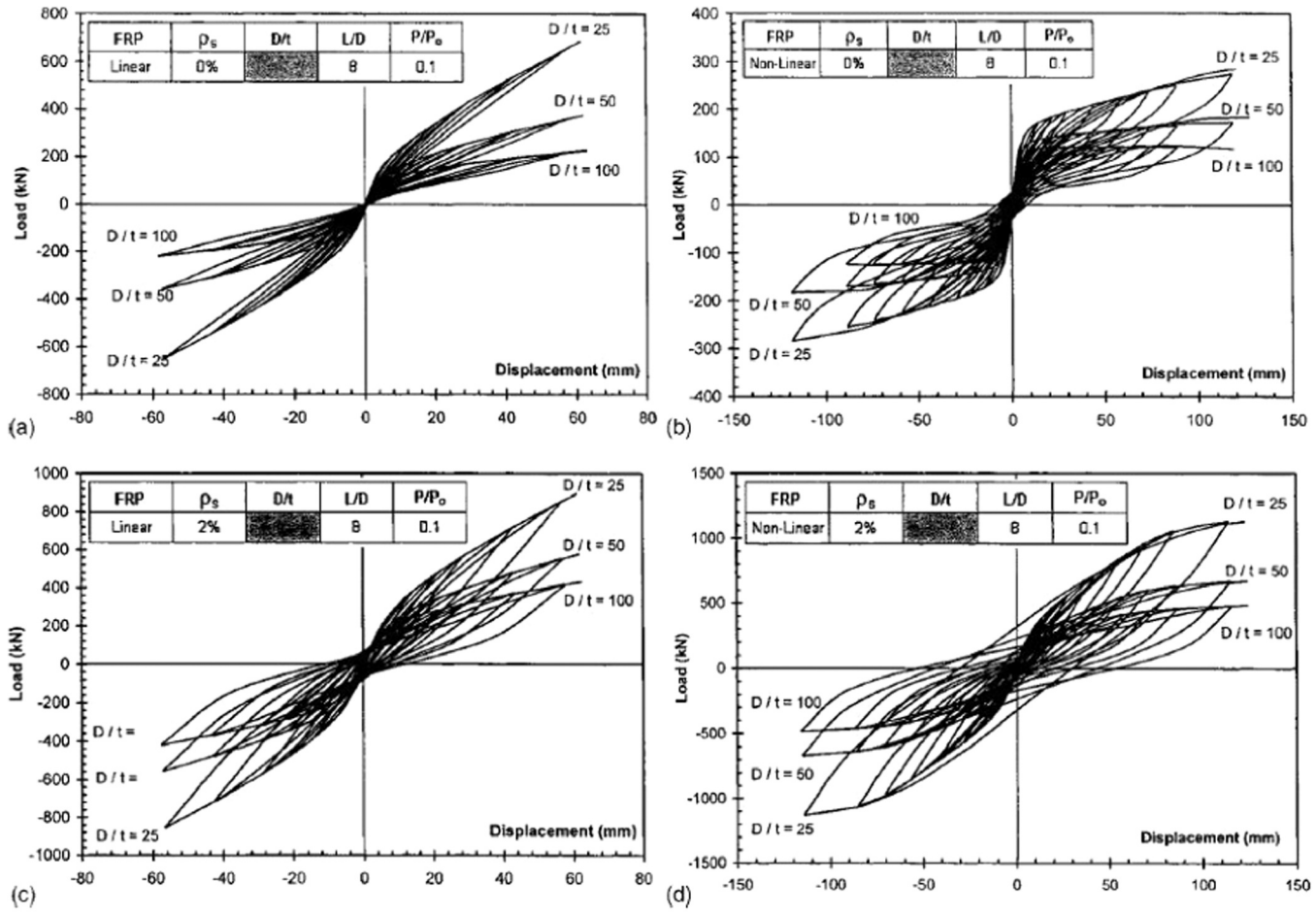

Fig. 69. Load-displacement: (a) Linear FRP (b) Non-linear FRP (Both had non-internal steel), (c) Linear FRP (d) Non-linear FRP (Both had internal steel) [76].

due to the initial potential of early shear failure to occur. Short column had high initial stiffness and less yield deflection. Hence, the declining L/D ratio inclined the beam ductility. Subsequently, L/D ratio had less effect and sometimes unaffected the pinching zone area.

A 2D three-node combined the fibre element with 14^0 of freedom was used to produce a large displacement of non-linear inelastic analysis on CFFT beam-columns, FRP, and steel cyclic constitutive models formed from the NM analysis that was performed using ABAQUS software. The NM considered two groups of FRP composite materials, which were linear and non-linear. Seven CFFT beam columns consisting of and without internal steel reinforcement were cyclically tested to ensure the model precision. In addition, the experimental findings agreed well with the fibre element, proving its resilience for inelastic cyclic analysis. They compared the CFST's hysteretic reaction of RC and CFST in order to observe and investigate how different CFFT parameters affected the NM response. As a result, CFFT columns might be reliably used and designed to achieve hysteretic performance levels similar to RC columns. The hysteretic reaction of CFFT columns could not compete with CFST columns unless their longer lifespan was considered before running the NM analysis.

6. Conclusion

The following primary conclusions were established based on reviewing various published experimental studies and finite element modelling of fibre reinforced polymer reinforced concrete beams (FRPRCB).

6.1. Experimental investigation

(1) The stress zone surrounding large gaps in unstrengthened beams exhibits an abnormal number of flexural fractures, which occur during flexure failure. The beam strength drops to 49%, including the stiffness drops to 20% when a huge square opening is added to RCB. Furthermore, the beam deflection rises by 31% due to the wide circular aperture during shear and flexure compared to the control beam without FRP reinforcement.

(2) Based on the experimental findings, using FRP composite materials as reinforcement is one of the most effective ways to strengthen RCB. The use of FRP is to increase the RCB's rigidity and load capacity. The structural performance and serviceability metrics are improved by considering the FRP anchoring. By increasing the usage of FRP, the stiffness and rigidity of the RCB structural members can be improved, preventing crushing or sudden failure of the RCB structural members. As a result, FRP boosts the RCB strength, including providing extra load-bearing capacity by considering the anchoring, rigidity, and stiffness of the RCB.

(3) GFRP is the most popular and widely used due to its lowest price among the other FRP composite materials available because GFRP is inferior reinforcement usage in RCB. BFRP is more expensive than GFRP. Despite its expensive price, AFRP's limited compressive strength means it is not frequently used as reinforcement for RCB. Compared to other FRP composite materials, CFRP is the most expensive because of its exceptional strength and resistance to fatigue and creep failures. The data shown in this review make it abundantly evident that FRP is becoming

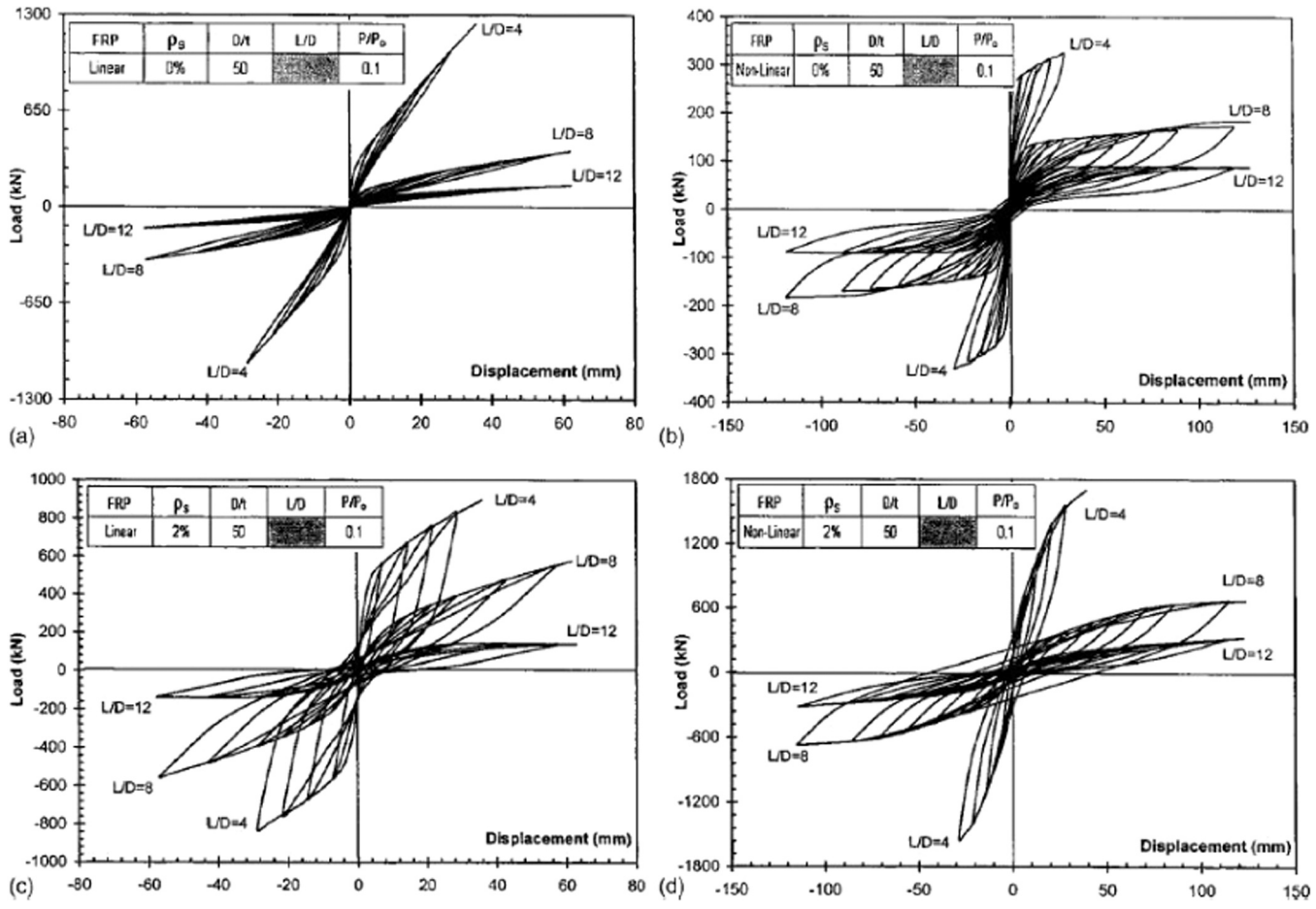

Fig. 70. Load-displacement: (a) Linear FRP (b) Non-linear FRP (Both had non-internal steel), (c) Linear FRP (d) Non-linear FRP (Both had internal steel) [76].

increasingly popular in civil engineering, especially since it has various types and is in high demand in construction industry. The FRP usage can undoubtedly be used for strengthening, repairing, and retrofitting building structural components such as beams, columns, slabs, and the like for several years.

6.2. Finite element analysis

(1) Multiple failure modes of FRPRCB in experimental study can be proven by using NM, which is dependent on FRP's shape and stiffness. High concentration stress in the area between concrete and FRP resulted in debonding, which is a common failure mechanism in RCB. Accordingly, minimising stress concentration is a crucial consideration in FRP reinforcement design. The stress concentration at the end plate will be more noticeable if FRP is stiff or narrow. Debonding occurs before steel yielding, while RCB failure occurs when a low load is imposed. Therefore, it is best to prevent this from occurring at all costs.

(2) The NM reliably forecasts the overall mechanical and structural performance of RCB reinforced with FRP composite material under negative moment applied. The NM results using finite element calculations that focusing the interface slip effect are almost similar and well agreed with the experimental values. The NM has greater non-linear stiffness than the experimental data because it assumes a perfect connection between FRP reinforcement and concrete. Also, it ignores the weakening influence of shear connectors in RCB reinforced by FRP composite material.

(3) FRP is deeply reviewed in this review article. A straightforward and effective 2D frame NM can faithfully maximise the structural properties of RCB, which has been flexural reinforced with externally bonded FRP laminates. The FRPRCB is created from force-based NM formulation standards, which distribute the FRP plasticity, stiffness, and ductility properties by discretising the FRP layer cross sections. On the other hand, FRPRCB may simulate many failure modes acquired in the actual construction world, like concrete crushing, steel yielding, FRP debonding and rupture at end plates, and debonding caused by intermediate crack propagation. Last but not least, the NM can simulate various FRP anchoring systems in order to strengthen the RCB strength further prior to concrete crushing and FRP debonding.

Declaration of Competing Interest

The authors declare that they have no known competing financial interests or personal relationships that could have appeared to influence the work reported in this paper.

References

[1] C.E. Bakis, L.C. Bank, V.L. Brown, E. Cosenza, J.F. Davalos, J.J. Lesko, A. Machida, S.H. Rizkalla, T.C. Triantafillou, Fiber-reinforced polymer composites for construction—state-of-the-art review, J. Compos. Constr. 6 (2) (2002) 73–87.
[2] W.D. Charles, FRP Pre-stressing in the USA, Concr. Int. 21 (10) (1999) 21–24.
[3] T. Luc, M. Stijn, FRP for concrete construction: activities in Europe, Concr. Int. 21 (10) (1999) 33–36.
[4] F. Hiroshi, FRP Composites in Japan, Concr. Int. 21 (10) (1999) 29–32.
[5] Task Group 9.3, FRP reinforcement in RC structures; No. 40, Federal Institute of Technology Lausanne, Switzerland, 2007.
[6] CSA S807, Specification for fibre-reinforced polymers. Canadian Standards Association (CSA): Mississauga, Ont, 2019, p. 67.

[7] R. Al-Sunna, K. Pilakoutas, I. Hajirasouliha, M. Guadagnini, Deflection behaviour of FRP reinforced concrete beams and slabs: an experimental investigation, Compos. B Eng. 43 (5) (2012) 2125–2134.
[8] A. Siddika, M.A.A. Mamun, W. Ferdous, R. Alyousef, Performances, challenges and opportunities in strengthening reinforced concrete structures by using FRPs – a state-of-the-art review, Eng. Fail. Anal. 111 (2020) 104480, https://doi.org/10.1016/j.engfailanal.2020.104480.
[9] S.S. Weli, I.S. Abbood, K.F. Hasan, M.A. Jasim, Effect of steel fibers on the concrete strength grade: a review, IOP Conf. Ser. Mater. Sci. Eng. 888 (2020) 012043, https://doi.org/10.1088/1757-899X/888/1/012043.
[10] E. Gudonis, et al., FRP reinforcement for concrete structures: state-of-the-art review of application and design, Eng. Struct. Technol. 5 (4) (2013) 147–158, https://doi.org/10.3846/2029882X.2014.889274.
[11] A. Ahmed, S. Guo, Z. Zhang, C. Shi, D. Zhu, A review on durability of fiber reinforced polymer (FRP) bars reinforced seawater sea sand concrete, Constr. Build. Mater. 256 (2020) 119484, https://doi.org/10.1016/j.conbuildmat.2020.119484.
[12] A. Carolin, Carbon fibre reinforced polymers for strengthening of structural elements Doctoral Thesis, Luleå University of Technology, Luleå, 2003, urn: nbn:se:ltu:diva-16879.
[13] Y.H. Mugahed Amran, R. Alyousef, R.S.M. Rashid, H. Alabduljabbar, C.-C. Hung, Properties and applications of FRP in strengthening RC structures: a review, Structures 16 (2018) 208–238.
[14] Solahuddin Bin Azuwa, The Effect of Shredded Paper as Partial Sand Replacement on Properties of Cement Sand Brick, Bachelor's Degree Thesis, Universiti Malaysia Pahang, Malaysia, 2017.
[15] B.A. Solahuddin, F.M. Yahaya, Effect of shredded waste paper on properties of concrete, IOP Conf. Ser.: Mater. Sci. Eng. 1092 (1) (2021) 012063, https://doi.org/10.1088/1757-899x/1092/1/012063.
[16] B.A. Solahuddin, F.M. Yahaya, Load-strain behaviour of shredded waste paper reinforced concrete beam, IOP Conf. Ser. Mater. Sci. Eng. 1092 (1) (2021) 012063, https://doi.org/10.1088/1757-899x/1092/1/012063.
[17] B.A. Solahuddin, F.M. Yahaya, A review paper on the effect of waste paper on mechanical properties of concrete, IOP Conf. Ser.: Mater. Sci. Eng. 1092 (1) (2021) 012063, https://doi.org/10.1088/1757-899x/1092/1/012067.
[18] B.A. Solahuddin, F.M. Yahaya, Structural behaviour of shredded waste paper reinforced concrete beam, Int. J. Adv. Res. Eng. Innov. 3 (1) (2021) 74–87. ⟨https://myjms.mohe.gov.my/index.php/ijarei/article/view/12968⟩.
[19] B.A. Solahuddin, F.M. Yahaya, Inclusion of waste paper on concrete properties: a review, Civ. Eng. J. -Tehran 7 (Special Issue-Innovative Strategies in Civil Engineering Grand Challenges)) (2021) 94–113, https://doi.org/10.28991/CEJ-SP2021-07-07.
[20] B.A. Solahuddin, A critical review on experimental investigation and finite element analysis on structural performance of kenaf fibre reinforced concrete, Structures 35 (November 2021)) (2022) 1030–1061, https://doi.org/10.1016/j.istruc.2021.11.056.
[21] B.A. Solahuddin, F.M. Yahaya, Properties of concrete containing shredded waste paper as an additive, Mater. Today.: Proc. 51 (2022) 1350–1354, https://doi.org/10.1016/j.matpr.2021.11.390.
[22] B.A. Solahuddin, A review on structural performance of bamboo reinforced concrete, Mater. Sci. Forum 1056 MSF (2022) 75–80, https://doi.org/10.4028/p-dx1×87.
[23] B.A. Solahuddin, Strengthening of reinforced concrete with steel fibre: a review, Mater. Sci. Forum 1056 (2017) (2022) 81–86, https://doi.org/10.4028/p-3g0h57.
[24] Solahuddin, B.A. (2022). A Review on The Effect of Reinforcement on Reinforced Concrete Beam-Column Joint Behavior. Proceedings of Malaysian Technical Universities Conference on Engineering and Technology (MUCET) 2021. ⟨https://crim.utem.edu.my/wp-content/uploads/2022/09/103-209-2101.pdf⟩.
[25] Solahuddin, B.A. (2022). Seismic Performance of Reinforced Concrete Beam-Column Joint: A Review. Proceedings of Malaysian Technical Universities Conference on Engineering and Technology (MUCET) 2021. ⟨https://crim.utem.edu.my/wp-content/uploads/2022/09/104-211-2121.pdf⟩.
[26] B.A. Solahuddin, A comprehensive review on waste paper concrete, Results Eng. 16 (October)) (2022) 100740, https://doi.org/10.1016/j.rineng.2022.100740.
[27] B.A. Solahuddin, F.M. Yahaya, A state-of-the-art review on experimental investigation and finite element analysis on structural behaviour of fibre reinforced polymer reinforced concrete beams, Heliyon 9 (3) (2023) e14225, https://doi.org/10.1016/j.heliyon.2023.e14225.
[28] B.A. Solahuddin, F.M. Yahaya, A narrative review on strengthening of reinforced concrete beams using carbon fibre reinforced polymer composite material through experimental investigation and numerical modelling, Structures 52 (January)) (2023) 666–710, https://doi.org/10.1016/j.istruc.2023.03.168.
[29] B.A. Solahuddin, F.M. Yahaya, Properties of concrete and structural behaviour of reinforced concrete beam containing shredded waste paper as an additive, Int J. Concr. Struct. Mater. 17 (2023) 26, https://doi.org/10.1186/s40069-023-00588-2.
[30] S. Bin Azuwa, F. Bin Mat Yahaya, Case study of block 1, highland towers condominium collapsed in Taman Hillview, Ulu Klang, Selangor, Malaysia on 11th December 1993, Alex. Eng. J. 85 (October)) (2023) 86–103, https://doi.org/10.1016/j.aej.2023.11.028.
[31] S. Bin Azuwa, A review on experimental observation on structural performance of bamboo reinforced concrete beam, Heliyon 10 (2) (2024) e24628, https://doi.org/10.1016/j.heliyon.2024.e24628.
[32] S.C. Chin, N. Shafiq, M.F. Nuruddin, 2011, , Strengthening of RC Beams Containing Large Opening at Flexure with CFRP laminates 5 (12743–749).
[33] C.A. Issa, A. AbouJouadeh, Carbon fiber reinforced polymer strengthening of reinforced concrete beams: experimental study, J. Archit. Eng. *10* (4) (2014) 121–125, https://doi.org/10.1061/(asce)1076-0431(2004)10:4(121).
[34] I.S. Abbood, S.A. Odaa, K.F. Hasan, M.A. Jasim, Properties evaluation of fiber reinforced polymers and their constituent materials used in structures - a review, Mater. Today.: Proc. *43* (2021) 1003–1008, https://doi.org/10.1016/j.matpr.2020.07.636.
[35] A. Siddika, M.A. Al Mamun, R. Alyousef, Y.H.M. Amran, Strengthening of reinforced concrete beams by using fiber-reinforced polymer composites: a review, J. Build. Eng. *25* (May)) (2019) 100798, https://doi.org/10.1016/j.jobe.2019.100798.
[36] Fischer, G.D. (2020). Deformation behavior of reinforced ECC flexural members under reversed cyclic loading conditions. *ProQuest Dissertations and Theses*, *Ph.D.* (100), 25–35. ⟨http://sfx.scholarsportal.info/western?url_ver=Z39.88-2004&rft_val_fmt=info:ofi/fmt:kev:mtx:dissertation&genre=dissertations+%26+theses&sid=ProQ:ProQuest+Dissertations+%26+Theses+Full+Text&atitle=&title=Deformation+behavior+of+reinforced+ECC+flexural⟩+.
[37] M. Mousay, Y.Y. Chai, S.I. Doh, K.S. Lim, Degradation of glass fiber reinforced polymer (GFRP) material exposed to tropical atmospheric condition, Key Eng. Mater., *879 KEM* (2021) 265–274, https://doi.org/10.4028/www.scientific.net/KEM.879.265.
[38] Springolo, M. (2015). *New fibre-reinforced polymer box beam: investigation of static behaviour*. *Civil*. ⟨https://eprints.usq.edu.au/1513/⟩.
[39] Polymer, R., For, C., Of, S., & Members, C. (2019). *A STUDY ON SUSTAINABLE AND ECO-FRIENDLY FIBER*.
[40] C. Pellegrino, C. Modena, Fiber-reinforced polymer shear strengthening of reinforced concrete beams: experimental study and analytical modeling, Acids Struct. J. *103* (5) (2016) 720–728, https://doi.org/10.14359/16924.
[41] T. Ovitigala, M.A. Ibrahim, M.A. Issa, Serviceability and ultimate load behavior of concrete beams reinforced with basalt fiber-reinforced polymer bars, Acids Struct. J. *113* (4) (2016) 757–768, https://doi.org/10.14359/51688752.
[42] E. Gudonis, E. Timinskas, V. Gribniak, G. Kaklauskas, A.K. Arnautov, V. Tamulėnas, Frp reinforcement for concrete structures: state-of-the-art review of application and design, Eng. Struct. Technol. 5 (2014) 147–158, https://doi.org/10.3846/2029882X.2014.889274.
[43] A. Ghobarah, M.N. Ghorbel, S.E. Chidiac, Upgrading torsional resistance of reinforced concrete beams using fiber-reinforced polymer, J. Compos. Constr. 6 (2002) 257–263, https://doi.org/10.1061/(ASCE)1090-0268(2002)6:4(257).
[44] R. Al-Rousan, Influence of opening sizes on the flexural behavior of heat-damaged reinforced concrete slabs strengthened with CFRP ropes, Case Stud. Constr. Mater. 17 (June)) (2022) e01464, https://doi.org/10.1016/j.cscm.2022.e01464.
[45] Rajai Z. Al-Rousan, Influence of macro synthetic fibers on the flexural behavior of reinforced concrete slabs with opening, Civ. Eng. J. 8 (9) (2022) 2001–2021, https://doi.org/10.28991/CEJ-2022-08-09-016.
[46] M. Alhassan, R. Al-Rousan, A. Ababneh, Anchoring of the main CFRP sheets with transverse CFRP strips for optimum upgrade of RC Beams: parametric experimental study, Constr. Build. Mater. 293 (2021) 123525, https://doi.org/10.1016/j.conbuildmat.2021.123525.
[47] M. Alhassan, R. Al-Rousan, A. Ababneh, Flexural behavior of lightweight concrete beams encompassing various dosages of macro synthetic fibers and steel ratios, Case Stud. Constr. Mater. 7 (July)) (2017) 280–293, https://doi.org/10.1016/j.cscm.2017.09.004.
[48] R. Al-Rousan, Influence of polypropylene fibers on the flexural behavior of reinforced concrete slabs with different opening shapes and sizes, Struct. Concr. 18 (6) (2017) 986–999, https://doi.org/10.1002/suco.201600222.
[49] R.Z. Al-Rousan, M.A. Issa, Flexural behavior of RC beams externally strengthened with CFRP composites exposed to severe environment conditions, KSCE J. Civ. Eng. 21 (2017) 2300–2309, https://doi.org/10.1007/s12205-016-0570-x.
[50] R.Z. Al-Rousan, Effect of CFRP schemes on the flexural behavior of RC beams modeled by using a nonlinear finite-element analysis, Mech. Compos. Mater. 51 (4) (2015) 437–446, https://doi.org/10.1007/s11029-015-9515-6.
[51] Rajai Z. Al-Rousan, Impact of Internal CFRP strips on the flexural behavior of heat-damaged reinforced concrete beams, Heliyon 9 (6) (2023) e17145, https://doi.org/10.1016/j.heliyon.2023.e17145.
[52] Rajai Z. Al-Rousan, Anchored CFRP ropes for flexural capacity recovering of thermally damaged RC one-way slabs, Alex. Eng. J. 76 (2023) 757–774, https://doi.org/10.1016/j.aej.2023.06.086.
[53] Rajai Z. Al-Rousan, The behavior of heated damaged shear-deficient RC beams reinforced internally with welded wire mesh, Case Stud. Constr. Mater. 15 (June)) (2021) e00687, https://doi.org/10.1016/j.cscm.2021.e00687.
[54] Rajai Z. Al-Rousan, Integration of CFRP strips as an internal shear reinforcement in reinforced concrete beams exposed to elevated temperature, Case Stud. Constr. Mater. 14 (2021) e00508, https://doi.org/10.1016/j.cscm.2021.e00508.
[55] Rajai Z. Al-Rousan, Impact of elevated temperature and anchored grooves on the shear behavior of reinforced concrete beams strengthened with CFRP composites, Case Stud. Constr. Mater. 14 (2021) e00487, https://doi.org/10.1016/j.cscm.2021.e00487.
[56] L. Amaireh, R.Z. Al-Rousan, A.N. Ababneh, M. Alhassan, Integration of CFRP strips as an internal shear reinforcement in reinforced concrete beams, Structures 23 (August 2019)) (2020) 13–19, https://doi.org/10.1016/j.istruc.2019.10.009.
[57] A. Ababneh, R. Al-Rousan, M. Alhassan, M. Alqadami, Influence of synthetic fibers on the shear behavior of lightweight concrete beams, Adv. Struct. Eng. 20 (11) (2017) 1671–1683, https://doi.org/10.1177/1369433217691773.
[58] Rajai Z. Al-Rousan, Shear behavior of RC beams externally strengthened and anchored with CFRP composites, Struct. Eng. Mech. 63 (4) (2017) 447–456, https://doi.org/10.12989/sem.2017.63.4.447.

[59] R.Z. Al-Rousan, M.A. Issa, The effect of beam depth on the shear behavior of reinforced concrete beams externally strengthened with carbon fiber–reinforced polymer composites, Adv. Struct. Eng. 19 (11) (2016) 1769–1779, https://doi.org/10.1177/1369433216649386.
[60] M.J. Shannag, R. Al-Rousan, Shear strengthening of high-strength reinforced concrete beams using fibrous composites, Mag. Concr. Res. 56 (7) (2004) 419–428, https://doi.org/10.1680/macr.2004.56.7.419.
[61] Rajai Z. Al-Rousan, B.R. Alnemrawi, Punching shear code provisions examination against the creation of an opening in existed RC flat slab of various sizes and locations, Structures 49 (February)) (2023) 875–888, https://doi.org/10.1016/j.istruc.2023.02.007.
[62] R. Al-Rousan, Influence of opening sizes on the flexural behavior of heat-damaged reinforced concrete slabs strengthened with CFRP ropes, Case Stud. Constr. Mater. 17 (June)) (2022) e01464, https://doi.org/10.1016/j.cscm.2022.e01464.
[63] R.Z. Alrousan, B.R. Alnemrawi, Punching shear behavior of FRP reinforced concrete slabs under different opening configurations and loading conditions, Case Stud. Constr. Mater. 17 (July)) (2022) e01508, https://doi.org/10.1016/j.cscm.2022.e01508.
[64] R. Rajai Al-Rousan, Influence of polypropylene fibers on the flexural behavior of reinforced concrete slabs with different opening shapes and sizes, Struct. Concr. 18 (6) (2017) 986–999, https://doi.org/10.1002/suco.201600222.
[65] Rajai Z. Al-Rousan, M.A. Alhassan, E.A. AlShuqari, Behavior of plain concrete beams with DSSF strengthened in flexure with anchored CFRP sheets—Effects of DSSF content on the bonding length of CFRP sheets, Case Stud. Constr. Mater. 9 (2018) e00195, https://doi.org/10.1016/j.cscm.2018.e00195.
[66] Rajai Z. Al-Rousan, Behavior of macro synthetic fiber concrete beams strengthened with different CFRP composite configurations, J. Build. Eng. 20 (April)) (2018) 595–608, https://doi.org/10.1016/j.jobe.2018.09.009.
[67] M.A. Alhassan, R.Z. Al-Rousan, L.K. Amaireh, M.H. Barfed, Nonlinear finite element analysis of B-C connections: influence of the column axial load, jacket thickness, and fiber dosage, Structures 16 (June)) (2018) 50–62, https://doi.org/10.1016/j.istruc.2018.08.011.
[68] Rajai Z. Al-Rousan, Empirical and NLFEA prediction of bond-slip behavior between DSSF concrete and anchored CFRP composites, Constr. Build. Mater. 169 (2018) 530–542, https://doi.org/10.1016/j.conbuildmat.2018.03.013.
[69] R.Z. Al-Rousana, Failure analysis of polypropylene fiber reinforced concrete two-way slabs subjected to static and impact load induced by free falling mass, Lat. Am. J. Solids Struct. 15 (1) (2018) 1–19, https://doi.org/10.1590/1679-78254895.
[70] M. Alhassan, R. Al-Rousan, A. Ababneh, Flexural behavior of lightweight concrete beams encompassing various dosages of macro synthetic fibers and steel ratios, Case Stud. Constr. Mater. 7 (July)) (2017) 280–293, https://doi.org/10.1016/j.cscm.2017.09.004.
[71] Obaidat, Y.T. (2022). *Structural retrofitting of reinforced concrete beams using carbon fibre reinforced polymer*.
[72] A. Song, H. Xu, Q. Luo, S. Wan, Finite element analysis on inelastic mechanical behavior of composite beams strengthened with carbon-fiber-reinforced polymer laminates under negative moment, Front. Mater. 9 (May)) (2022) 1–13, https://doi.org/10.3389/fmats.2022.859663.
[73] M. Barbato, Efficient finite element modelling of reinforced concrete beams retrofitted with fibre reinforced polymers, Comput. Struct. *87* (3–4) (2019) 167–176, https://doi.org/10.1016/j.compstruc.2008.11.006.
[74] M.M. Rafi, A. Nadjai, F. Ali, Finite element modeling of carbon fiber-reinforced polymer reinforced concrete beams under elevated temperatures, Acids Struct. J. *105* (6) (2018) 701–710, https://doi.org/10.14359/20098.
[75] N. Manish Kumar, S. Sameer, K. Divya, Numerical simulations of composite materials, IOP Conf. Ser.: Earth Environ. Sci. 982 (1) (2022), https://doi.org/10.1088/1755-1315/982/1/012019.
[76] Y. Shao, S. Aval, A. Mirmiran, Fiber-element model for cyclic analysis of concrete-filled fiber reinforced polymer tubes, J. Struct. Eng. *131* (2) (2015) 292–303, https://doi.org/10.1061/(asce)0733-9445(2005)131:2(292).